Lattice Boltzmann method for contact-line motion of binary fluids with high density ratio

Hong Liang,[1] Haihu Liu,[2] Zhenhua Chai,[3,*] and Baochang Shi[3]
[1]*Department of Physics, Hangzhou Dianzi University, Hangzhou 310018, China*
[2]*School of Energy and Power Engineering, Xian Jiaotong University, Xian 710049, China*
[3]*School of Mathematics and Statistics, Huazhong University of Science and Technology, Wuhan 430074, China*

(Received 14 January 2019; published 12 June 2019)

Within the phase-field framework, we present an accurate and robust lattice Boltzmann (LB) method for simulating contact-line motion of immiscible binary fluids on the solid substrate. The most striking advantage of this method lies in that it enables us to handle two-phase flows with mass conservation and a high density contrast of 1000, which is often unavailable in the existing multiphase LB models. To simulate binary fluid flows, the present method utilizes two LB evolution equations, which are respectively used to solve the conservative Allen-Cahn equation for interface capturing, and the incompressible Navier-Stokes equations for hydrodynamic properties. Besides, to account for the substrate wettability, two popular contact angle models including the cubic surface-energy model and the geometrical one are incorporated into the present method, and their performances are numerically evaluated over a wide range of contact angles. The contact-angle hysteresis effect, which is inherent to a rough or chemically inhomogeneous substrate, is also introduced in the present LB approach through the strategy proposed by Ding and Spelt [J. Fluid Mech. **599**, 341 (2008)]. The present method is first validated by simulating droplet spreading and capillary intrusion on the ideal or smooth pipes. It is found that the cubic surface-energy and geometrical wetting schemes both offer considerable accuracy for predicting a static contact angle within its middle region, while the former is more stable at extremely small contact angles. Besides, it is shown that the geometrical wetting scheme enables us to obtain better accuracy for predicting dynamic contact points in capillary pipe. Then we use the present LB method to simulate the droplet shearing processes on a nonideal substrate with contact angle hysteresis. The geometrical wetting model is found to be capable of reproducing four typical motion modes of contact line, while the surface-energy wetting scheme fails to predict the hysteresis behaviors in some cases. At last, a complex contact-line dynamic problem of three-dimensional microscale droplet impact on a wettable solid is simulated, and it is found that the numerical results for droplet shapes agree well with the experimental data.

DOI: 10.1103/PhysRevE.99.063306

I. INTRODUCTION

When the mixture of two immiscible fluids encounters a solid substrate, a moving contact line forms on it where fluid interface intersects the solid surface. These typical wall-bounded two-phase flows are omnipresent in nature and practical engineering applications, such as water droplet slipping or rolling on leaves, spray coating processes, enhanced oil recovery, water transport in fuel cells, and droplet manipulation in microfluidic devices [1]. Due to its wide and important applications, the contact-line dynamic has long been of interest to the fluid research community [2–5]. In spite of intensive theoretical and experimental studies [2–4], numerical modeling has become an increasingly efficient approach with the great advances in computer power, while some challenges still remain. The reasons behind the difficulties lie in the aspects of the moving contact-line problem such as complex interactions among fluids and solid, surface tension force modeling, and large density or viscosity change across the interface of liquid and gas phases. Several traditional numerical methods, including the level set method [6], spectral boundary element method [7], volume-of-fluid method [8], and boundary-integral method [9] have been developed for simulating the contact-line dynamics. In these methods, some extra efforts such as interface reconstruction or reinitialization are required to correct phase interface at every evolution step. Besides, they would suffer from the drawback that an empirical slip model with a slip length on solid surface should be imposed to overcome the stress singularity at the moving contact line [10,11]. Following a different path, the mesoscopic lattice Boltzmann (LB) method [12,13] is the kinetic-theory based method, which evolves the particle distribution function and the macroscopic quantities are solved by the moment integrations of the distribution function. This kinetic characteristic of the LB method has made it become a promising tool for complex hydrodynamic phenomena [14,15] and in particular for multiphase flows [16–22].

Several types of multiphase LB models have been constructed from different physical perspectives of the interactions, which commonly include the color-gradient model [16], pseudopotential model [17], free-energy model [18], phase-field based model [19–22], and off-lattice LB model [23]. All these models have their own impressive versatility in simulating two-phase flows and are also widely employed to study the moving contact-line problems. It is well known that the

*Corresponding author: hustczh@hust.edu.cn

wettability of solid substrate plays a vital role in the determination of contact line dynamics and thus how to implement solid surface wetting property in terms of the microscale contact angle into the LB approach is a crucial problem. The earliest exploration was carried out by Martys and Chen [24], who introduced a fluid-solid interaction in the pseudopotential LB model [17] to describe surface wettability and the contact angle can be achieved through adjusting the interaction strength. Using this wetting scheme, they successfully simulated the displacement of one fluid by another density-matched fluid in a porous medium. Inspired by this work, several different forms of fluid-solid interactions [25–27] have been sequentially formulated within the framework of the pseudopotential model, and were also used to simulate the contact-line dynamics on the smooth or chemically patterned substrate with the density ratios less than 30 [25,26,28–30] and up to 500 [27]. The advantage of this type of wetting formulation is that it can be easily generalized to other LB multiphase models [31,32]. Nevertheless, it also has the deficiency that the equilibrium contact angle cannot be prescribed in advance, but instead is determined by a prior simulation. In addition, by specifying a constant wall density, a layer of unphysical film would appear on the solid surface. Based on the surface free energy of Cahn theory [33], Briant *et al.* [34,35] proposed another type of wetting scheme known as the surface-energy formulation in the free-energy LB model, and employed the approach to simulate the contact-line motion of nonideal gases and binary fluids with density ratios smaller than 5. The idea of this scheme lies in the wetting behavior of fluids on a solid surface described by a wall free-energy functional that represents the fluid-solid interaction, and the surface free-energy functional is expanded into a power series of the density. The linear approximation of the wall free-energy functional was originally adopted by Briant and co-workers [34,35] within the framework of free-energy LB model [18] and was later used in the phase-field based LB model [36]. The distinct feature of this wetting scheme is that the microscale contact angle can be known beforehand as an input simulation parameter without an additional simulation, which seems to be rather efficient for studying partial wetting problems [34,35,37–40]. However, the theoretical analysis indicated that the unphysical phenomenon of spurious film layer on a solid surface also exists in this wetting treatment [41]. To settle this problem, an improved wetting boundary scheme with a cubic form of wall free-energy functional was proposed by Wiklund *et al.* [41]. They coupled it with a binary free-energy LB model [18] to study the wetting problems with the density-matched fluids. It was reported that the cubic wetting formulation, as compared to the linear one, enables to capture the wetting phenomena with higher accuracy and wider range of contact angles, and also can eliminate the spurious film at solid surface. By incorporating this wetting scheme into a Cahn-Hilliard phase-field LB model, Lee *et al.* [20] successfully simulated a microscale droplet impact on partial wetting solid with the high density ratio of 1000. The success access to the high density ratio is due to the use of a stable mixing difference method for computing gradient terms, which unfortunately could lead to the violation of global mass conservation [42]. The cubic surface-energy wetting formulation was also utilized by Lou *et al.* [43], who introduced it in an improved phase-field LB method for simulating the contact-line dynamics with a mild density ratio of around 10. From the perspective of force balance, Latva-Kokko and Rothman [44,45] extended the color-gradient LB model [16] to simulate the wetting phenomena in terms of static and dynamic contact angles with small density ratios. Recently, Wang *et al.* [46] implemented the geometric wetting formulation proposed by Ding *et al.* [11] in a phase-field based LB model [19], and verified the approach by simulating the droplet dynamic behaviors on the ideal wall, and also on the nonideal wall with the consideration of contact angle hysteresis. The numerical results showed that the proposed approach was suitable for simulating the contact-line problems with a density ratio of about 10. More recently, Liu and co-workers [47,48] proposed an improved color-gradient LB model for contact-line motions, while they only focused on a two-phase system of density-equal fluids.

As reviewed above, although several LB models have been proposed for simulating multiphase flows involving moving contact lines, the majority of them are limited to small or moderate density contrasts. Generally, the density ratio of liquid and gas is larger than 100, which even could approach 1000 for a realistic water-air two-phase system. Within this context, it is extremely desirable to develop a multiphase LB model that can simulate contact-line dynamics with high density ratio. To fill this gap, in this paper we attempt to present an efficient LB approach for simulating contact-line dynamics with the density ratio up to $O(10^3)$. Two popular cubic surface-energy and geometric wetting formulations are incorporated in the present method, and their numerical performances in terms of the predicted microscale contact angle and the maximum spurious velocity are evaluated in detail. The complex contact angle hysteresis phenomenon is also taken into consideration. The rest of the paper is arranged as follows. In Sec. II, we first briefly introduce a LB approach for two-phase flows based on the Allen-Cahn phase-field theory, and the wetting boundary scheme for contact angle and its hysteresis is then presented. Numerical experiments to validate the present method and detailed comparisons between the present numerical results with some available results can be found in Sec. III, and finally we present a brief summary in Sec. IV.

II. MATHEMATICAL METHOD

A. LB method for two-phase flows

The phase-field models [49,50] have become increasingly popular for simulating two-phase flows owing to its underlying physics in describing interfacial dynamics. To date, several LB multiphase models [20,21,51–53] have been constructed from the perspective of the phase-field theories, which can be divided into the Cahn-Hilliard [20,21] and the Allen-Cahn types [51–53]. The latter in contrast contains a lower-order derivative in its diffusion term which makes it computationally more efficient and less dispersive [51,52]. In this study, we employ the phase-field LB method recently improved by Liang *et al.* [52] because of its distinct advantage in handling immiscible multiphase flows with a high density ratio. The method utilizes two distribution functions, f_i and g_i,

which are respectively used to solve the conservative Allen-Cahn equation and the Navier-Stokes equations [52,54],

$$f_i(\mathbf{x}+\mathbf{c}_i\delta_t, t+\delta_t) - f_i(\mathbf{x},t) = -\frac{1}{\tau_f}[f_i(\mathbf{x},t) - f_i^{eq}(\mathbf{x},t)] + \delta_t F_i(\mathbf{x},t), \tag{1}$$

$$g_i(\mathbf{x}+\mathbf{c}_i\delta_t, t+\delta_t) - g_i(\mathbf{x},t) = -\frac{1}{\tau_g}[g_i(\mathbf{x},t) - g_i^{eq}(\mathbf{x},t)] + \delta_t G_i(\mathbf{x},t), \tag{2}$$

where $f_i(\mathbf{x},t)$, $g_i(\mathbf{x},t)$ are the particle distribution functions, $f_i^{eq}(\mathbf{x},t)$ and $g_i^{eq}(\mathbf{x},t)$ are the corresponding equilibrium distribution functions, τ_f and τ_g are the relaxation factors, F_i and G_i are the forcing distribution functions. To recover the target equations, the equilibrium distribution function f_i^{eq} can be defined by

$$f_i^{eq} = \omega_i\phi\left(1 + \frac{\mathbf{c}_i\cdot\mathbf{u}}{c_s^2}\right), \tag{3}$$

and g_i^{eq} can be given by

$$g_i^{eq} = \begin{cases} \frac{p}{c_s^2}(\omega_i - 1) + \rho s_i(\mathbf{u}), & i = 0, \\ \frac{p}{c_s^2}\omega_i + \rho s_i(\mathbf{u}), & i \neq 0 \end{cases} \tag{4}$$

with

$$s_i(\mathbf{u}) = \omega_i\left[\frac{\mathbf{c}_i\cdot\mathbf{u}}{c_s^2} + \frac{(\mathbf{c}_i\cdot\mathbf{u})^2}{2c_s^4} - \frac{\mathbf{u}\cdot\mathbf{u}}{2c_s^2}\right], \tag{5}$$

where $\mathbf{u}$ is the fluid velocity, ρ is the density, p is the pressure, c_s is the sound speed, $\mathbf{c}_i$ is the discrete velocity, and ω_i is the weighting coefficient. In Eq. (3), ϕ is an order parameter used to distinguish different fluids, which generally takes 1 and 0 in the liquid and gas bulk regions, and the two-phase interface can be represented by the contour level of $\phi = 0.5$. In the LB method, ω_i and $\mathbf{c}_i$ are determined by the lattice model. For commonly used lattice models in the two- and three-dimensional spaces, they can be defined as [55–57]

D2Q9:

$$\omega_0 = \frac{4}{9},\ \omega_{1-4} = \frac{1}{9},\ \omega_{5-8} = \frac{1}{36},\ c_s^2 = \frac{c^2}{3}, \tag{6a}$$

$$\mathbf{c}_i = \begin{pmatrix} 0 & 1 & 0 & -1 & 0 & 1 & -1 & -1 & 1 \\ 0 & 0 & 1 & 0 & -1 & 1 & 1 & -1 & -1 \end{pmatrix} c, \tag{6b}$$

D3Q7:

$$\omega_0 = \frac{1}{4},\ \omega_{1-6} = \frac{1}{8},\ c_s^2 = \frac{c^2}{4}, \tag{7a}$$

$$\mathbf{c}_i = \begin{pmatrix} 0 & 1 & -1 & 0 & 0 & 0 & 0 \\ 0 & 0 & 0 & 1 & -1 & 0 & 0 \\ 0 & 0 & 0 & 0 & 0 & 1 & -1 \end{pmatrix} c, \tag{7b}$$

D3Q15:

$$\omega_0 = \frac{2}{9},\ \omega_{1-6} = \frac{1}{9},\ \omega_{7-14} = \frac{1}{72},\ c_s^2 = \frac{c^2}{3}, \tag{8a}$$

$$c_i = \begin{pmatrix} 0 & 1 & -1 & 0 & 0 & 0 & 0 & 1 & -1 & 1 & -1 & 1 & -1 & 1 & -1 \\ 0 & 0 & 0 & 1 & -1 & 0 & 0 & 1 & 1 & -1 & -1 & 1 & 1 & -1 & -1 \\ 0 & 0 & 0 & 0 & 0 & 1 & -1 & 1 & 1 & 1 & 1 & -1 & -1 & -1 & -1 \end{pmatrix} c, \tag{8b}$$

where $c = \delta_x/\delta_t$ is the lattice speed, δ_x is the grid spacing, and δ_t is the time step. In this work, the popular D2Q9 lattice model is used for the simulation of the two-dimensional flows. For the three-dimensional flows, however, the efficient D3Q7 lattice model is applied in the LB evolution (1) for the Allen-Cahn equation, and the D3Q15 lattice model is adopted in the LB equation (2) for the Navier-Stokes equations. One main part of the diffusion term in the Allen-Cahn equation is regarded as the source term here, and then the forcing distribution function F_i is carefully designed as

$$F_i = \left(1 - \frac{1}{2\tau_f}\right)\frac{\omega_i\mathbf{c}_i\cdot\left[\partial_t(\phi\mathbf{u}) + c_s^2\frac{4\phi(1-\phi)}{W}\mathbf{n}\right]}{c_s^2}, \tag{9}$$

where W is the interface thickness, and $\mathbf{n}$ is the unit vector normal to the interface,

$$\mathbf{n} = \frac{\nabla\phi}{|\nabla\phi|}. \tag{10}$$

Besides, the force should also be prudently treated since it could produce the discrete lattice effect when incorporated into the LB approach [58]. We take into account this discrete lattice effect, and formulate a simple forcing distribution function G_i as

$$G_i = \left(1 - \frac{1}{2\tau_g}\right)\omega_i\left(\frac{\mathbf{c}_i\cdot\mathbf{F}}{c_s^2} + \frac{\mathbf{u}\nabla\rho:\mathbf{c}_i\mathbf{c}_i}{c_s^2}\right), \tag{11}$$

where $\mathbf{F}$ is the total force, including the surface tension force $\mathbf{F}_s$ and the external force $\mathbf{G}$,

$$\mathbf{F} = \mathbf{F_s} + \mathbf{G}, \tag{12}$$

where $\mathbf{F}_s$ takes the potential form of the phase-field model [59],

$$\mathbf{F}_s = \mu\nabla\phi, \tag{13}$$

where μ is the chemical potential and is a function of ϕ,

$$\mu = 4\beta\phi(\phi-1)(\phi-0.5) - k\nabla^2\phi, \tag{14}$$

where k and β are physical parameters determined by the given interface thickness and surface tension (σ),

$$k = \frac{3}{2}\sigma W,\ \beta = \frac{12\sigma}{W}. \tag{15}$$

In the diffuse interface numerical method, the interface has a nonzero width and the physical quantities are allowed to change smoothly across the interface. By experience, the sustainable interface thickness falls into the region between three and five lattice units, beyond which the algorithm becomes unstable or the interface shape may be distorted. Unless otherwise stated, the interface thickness W in a numerical simulation is set to four lattice units.

In the present model, the order parameter ϕ can be computed from the zeroth-order moment of the distribution function f_i,

$$\phi = \sum_i f_i, \tag{16}$$

and the fluid density takes the linear function of ϕ,

$$\rho = \phi(\rho_l - \rho_g) + \rho_g, \tag{17}$$

where ρ_l and ρ_g represent the densities of the liquid and gas phases. The other macroscopic quantities $\mathbf{u}$ and p can be derived from the distribution function g_i [21],

$$\rho\mathbf{u} = \sum_i \mathbf{c}_i g_i + 0.5\delta_t \mathbf{F}, \tag{18a}$$

$$p = \frac{c_s^2}{(1-\omega_0)}\left[\sum_{i\neq 0} g_i + \frac{\delta_t}{2}\mathbf{u}\cdot\nabla\rho + \rho s_0(\mathbf{u})\right]. \tag{18b}$$

Applying the Chapman-Enskog analysis to the LB equations (1) and (2), we can show that the Allen-Cahn equation

$$\frac{\partial\phi}{\partial t} + \nabla\cdot(\phi\mathbf{u}) = \nabla\cdot\left[M(\nabla\phi - \frac{4\phi(1-\phi)}{W}\mathbf{n})\right], \tag{19}$$

and the incompressible Navier-Stokes equations with the force,

$$\nabla\cdot\mathbf{u} = 0, \tag{20a}$$

$$\frac{\partial(\rho\mathbf{u})}{\partial t} + \nabla\cdot(\rho\mathbf{u}\mathbf{u}) = -\nabla p + \nabla\cdot[\nu\rho(\nabla\mathbf{u} + \nabla\mathbf{u}^T)] + \mathbf{F}, \tag{20b}$$

can be exactly recovered without any additional assumption. Besides, the relation between the mobility M and the relaxation factor is expressed as

$$M = c_s^2(\tau_f - 0.5)\delta t \tag{21}$$

and the kinematic viscosity ν is given by

$$\nu = c_s^2(\tau_g - 0.5)\delta_t. \tag{22}$$

In a two-phase system, the viscosity is no longer a uniform value due to its jump across the liquid-gas interface. Similar to the density field, one can adopt a simple linear function to determine the kinematic viscosity,

$$\nu = \phi(\nu_l - \nu_g) + \nu_g, \tag{23}$$

where ν_l and ν_g are the kinematic viscosities of the liquid and gas phases. Supposing that the physical variables ν_l and ν_g are constants, the viscosity in the whole computational domain can be given, and further the relaxation factor τ_g can be determined according to Eq. (22). Another popular method to treat the viscosity at the interface is the inverse linear form [20],

$$\frac{1}{\nu} = \phi\left(\frac{1}{\nu_l} - \frac{1}{\nu_g}\right) + \frac{1}{\nu_g}. \tag{24}$$

Oftentimes, the linear scheme for the dynamic viscosity is also used in the numerical modeling, while the numerical experiments indicate that such a treatment may induce the numerical instability, which will not be used in this study. In practice, some derivative terms in the LB evolution equations should be discretized with suitable difference schemes. The explicit Euler scheme is used to compute the temporal derivative in Eq. (9), i.e., $\partial_t(\phi\mathbf{u}) = [\phi(t)\mathbf{u}(t) - \phi(t-\delta_t)\mathbf{u}(t-\delta_t)]/\delta_t$, and the second-order isotropic central schemes are applied for the evaluation of gradient and Laplacian operators,

$$\nabla\phi(\mathbf{x}) = \sum_{i\neq 0}\frac{\omega_i\mathbf{c}_i\phi(\mathbf{x}+\mathbf{c}_i\delta_t)}{c_s^2\delta_t}, \tag{25}$$

$$\nabla^2\phi(\mathbf{x}) = \sum_{i\neq 0}\frac{2\omega_i[\phi(\mathbf{x}+\mathbf{c}_i\delta_t) - \phi(\mathbf{x})]}{c_s^2\delta_t^2}. \tag{26}$$

B. Wetting boundary conditions

When the two-phase fluids encounter with a solid substrate, the wettability of the substrate plays a vital role in influencing fluid interface dynamics. Thus it is necessary to formulate a wetting boundary condition that accounts for the contact angle between phase interface and solid surface. In this subsection, we will give the details on the construction of wetting boundary conditions from two different physical viewpoints and how they are implemented in the framework of the present model. First, the wetting boundary condition for two-phase flows can be constructed by considering an additional wall free-energy functional. Denoting the flow domain by V and its solid boundary by ∂V, the total Landau free-energy functional of a multiphase system can be expressed as [2,60]

$$\Psi = \int_V\left(E_0 + \frac{k}{2}|\nabla\phi|^2\right)dV + \int_{\partial V}\psi_s(\phi)ds, \tag{27}$$

where E_0 is the bulk free-energy density and is chosen to have a double-well form, i.e., $E_0 = \beta\phi^2(\phi-1)^2$, the term $\frac{k}{2}|\nabla\phi|^2$ accounts for the contribution of the excess free energy in the interfacial region, and $\psi_s(\phi)$ represents the free-energy density on the fluid-solid boundary. In the phase-field theory, the wetting boundary condition for two-phase flows can be derived by minimizing the total free energy. Applying the variational operator to the free-energy functional (27), one can obtain

$$\delta\Psi = \int_V\left(\frac{\partial E_0}{\partial\phi}\delta\phi + k\nabla\phi\cdot\delta(\nabla\phi)\right)dV + \int_{\partial V}\frac{\partial\psi_s}{\partial\phi}\delta\phi ds, \tag{28}$$

which can be further written as

$$\delta\Psi = \int_V \left(\frac{\partial E_0}{\partial\phi}\delta\phi - k\nabla^2\phi\delta\phi\right)dV + \int_V k\nabla\cdot(\nabla\phi)\delta\phi dV + \int_{\partial V}\frac{\partial\psi_s}{\partial\phi}\delta\phi ds,$$

$$= \int_V \left(\frac{\partial E_0}{\partial\phi} - k\nabla^2\phi\right)\delta\phi dV + \int_{\partial V}\left(-k\mathbf{n}_w\cdot\nabla\phi + \frac{\partial\psi_s}{\partial\phi}\right)\delta\phi ds, \tag{29}$$

where the Gauss integral theorem has been used, $\mathbf{n}_w$ represents the unit vector normal to the solid surface and has the direction pointing from solid toward the fluid. Taking the variational of the free energy to be zero leads to

$$-k\mathbf{n}_w\cdot\nabla\phi + \frac{\partial\psi_s}{\partial\phi} = 0, \tag{30}$$

which is the imposed wetting boundary condition if the wall free energy ψ_s is specified. In addition, another constraint condition in the bulk region can also be derived, but for convenience of the discussion, we assume one phase of nonideal fluids occupies the region $y > 0$ and the solid wall is located at $y = 0$. From Eq. (29), we can obtain the following two constraint conditions:

$$\frac{dE_0}{d\phi} = k\frac{d^2\phi}{dy^2}, \quad \text{for } y > 0, \tag{31a}$$

$$k\frac{d\phi}{dy} = \frac{d\psi_s}{d\phi}, \quad \text{for } y = 0. \tag{31b}$$

The substitution of a first integral result of Eq. (31a) into Eq. (31b) yields

$$\frac{d\psi_s}{d\phi} = \pm\sqrt{2kE_0}. \tag{32}$$

According to the wetting theory of Gennes [2], the wall free energy ψ_s can be expanded into the power series with respect to the order parameter,

$$\psi_s = a_0 - a_1\phi + a_2\phi^2 - a_3\phi^3 + \cdots. \tag{33}$$

Taking the linear form of the wall free energy, $\psi_s = -a_1\phi$, one can derive the linear wetting boundary condition for contact angle [34,37],

$$\mathbf{n}_w\cdot\nabla\phi = -\frac{a_1}{k}, \tag{34}$$

where a_1 is related to the dimensionless wetting potential by $\Omega = 4a_1/\sqrt{2k\beta}$, and Ω is a function of the contact angle with the relation

$$\Omega = 2\mathrm{sgn}\left(\frac{\pi}{2} - \theta\right)\left[\cos\frac{\alpha}{3}\left(1 - \frac{\cos\alpha}{3}\right)\right], \tag{35}$$

where $\alpha = \arccos(\sin^2\theta)$. For a given contact angle θ, we can uniquely determine the value of Ω and also the parameter a_1, and the imposed wetting condition given in Eq. (34) can be solved. This linear strategy we noted was widely adopted in the LB modeling [34–37] of the wetting phenomenon, and was also similar to those used in the pseudopotential model [24,25]. Unfortunately, when Eq. (34) is used to describe the wetting property, the order parameter at the solid wall will be constant and then a layer of spurious film could be produced at the solid surface. Another methodology using the high-order wall free energy can overcome this unphysical phenomenon. To construct the advanced wetting boundary condition, we neglect the interactions between solid and bulk phases, and only consider the interaction at the three-phase junction. To satisfy this assumption, the cubic wall free energy should take the following form: $\psi_s = \frac{b_1}{2}\phi^2 - \frac{b_1}{3}\phi^3$, where b_1 is a parameter. Substituting the new ψ_s into Eq. (30), a cubic wetting boundary condition can be derived,

$$k\mathbf{n}_w\cdot\nabla\phi = b_1(\phi - \phi^2). \tag{36}$$

In addition, it is found that Eq. (32) with the substitution of ψ_s has two stable solutions of $\phi_{s_1} = 0$ and $\phi_{s_2} = 1$. Then, the surface tensions for gas-solid and liquid-solid phases can be expressed by

$$\sigma_{sg} = \frac{b_1}{2}\phi_{s_1}^2 - \frac{b_1}{3}\phi_{s_1}^3 + \int_0^{\phi_{s_1}}\sqrt{2kE_0}d\phi = 0, \tag{37a}$$

$$\sigma_{sl} = \frac{b_1}{2}\phi_{s_2}^2 - \frac{b_1}{3}\phi_{s_2}^3 + \int_1^{\phi_{s_2}}\sqrt{2kE_0}d\phi = \frac{b_1}{6}. \tag{37b}$$

For the two-phase fluids on the chemically homogeneous wall, the surface wettability can be evaluated in terms of the contact angle, which is determined based on the Young's equation associated with the surface tensions at the three-phase junction, $\cos\theta = (\sigma_{sg} - \sigma_{sl})/\sigma$ [61]. Therefore, the contact angle can be evaluated as

$$\cos\theta = \frac{\sigma_{sg} - \sigma_{sl}}{\sigma} = -\frac{b_1}{\sqrt{2k\beta}}. \tag{38}$$

Using Eq. (38), one can ultimately obtain the cubic wetting boundary condition for two-phase flows in contact with solid,

$$\mathbf{n}_w\cdot\nabla\phi = -\sqrt{\frac{2\beta}{k}}\cos\theta(\phi - \phi^2). \tag{39}$$

From Eq. (39), it can be clearly seen that the gradient of the density in the bulk phases is zero and is nonzero only at the three-phase junction, which implies that the interaction between bulk phases and solid vanishes and the wetting condition only works at the liquid-gas-solid point, as expected. In addition, it is obvious that the wall density in bulk phases is equal to the value of the corresponding saturation state and thus the spurious film at the solid surface disappears.

Alternatively, Ding *et al.* [11] proposed a wetting boundary condition for simulating a contact-line problem from the viewpoint of the geometrical relation. Supposing a steady droplet on the solid substrate, the wetting boundary condition based on geometrical formulation can be expressed as

$$\mathbf{n}_w\cdot\nabla\phi = -\tan\left(\frac{\pi}{2} - \theta\right)|\mathbf{n}_\tau\cdot\nabla\phi|, \tag{40}$$

where $\mathbf{n}_\tau$ is the unit vector tangential to solid surface. In the two-dimensional case, the tangential component of $\nabla\phi$ can be written as $\frac{\partial\phi}{\partial x}$ and in the three-dimensional case, it can be expressed by $\sqrt{(\frac{\partial\phi}{\partial x})^2 + (\frac{\partial\phi}{\partial y})^2}$ [46]. Although the cubic

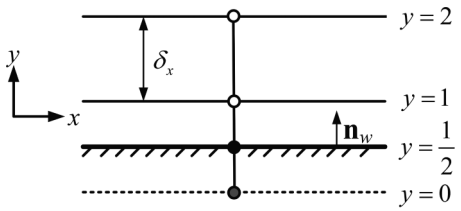

FIG. 1. Schematics of fluid lattice node and solid wall boundary.

surface-energy and geometric formulations seem to be significantly different in form, they are mathematically equivalent in computing contact angle for a given order parameter distribution [11]. On the other hand, it is important to note that they may behave differently for a prescribed contact angle in the numerical simulations. Both of them have been successfully applied to the LB simulation of fluid-solid wetting phenomena [20,41,43,46,48], but most of the models are only suitable to binary fluids with low or moderate density ratios. This work is devoted to implementing the wetting boundary conditions in our recently improved LB model and applying them to simulate wall-bounded two-phase flows with a large density ratio of 1000.

We now introduce how the two-phase wetting boundary conditions are implemented in the LB framework. In the present LB model, the gradient of the order parameter and its Laplacian operator can be evaluated using Eqs. (25) and (26). While for the fluid node neighboring to a solid wall, the computations of $\nabla\phi$ and $\nabla^2\phi$ need the information of ϕ beyond the fluid domain and thus should be specifically treated by imposing the wetting boundary condition. For the simplicity of discussion, we consider the case of a flat boundary. The fluid layers, ghost layer, and solid boundary are sketched in Fig. 1, where $y = 1$ is the fluid layer next to the solid boundary, $y = 0$ is the ghost cell, and $y = \frac{1}{2}$ represents the solid boundary that is located halfway between the fluid and ghost layers. In order to calculate the terms of $\nabla\phi$ and $\nabla^2\phi$, the macroscopic quantity at the ghost layer should be specified. Note that Eq. (39) is only imposed for the order parameter at the solid surface. Applying the second-order difference scheme, $\frac{\partial\phi}{\partial n_w} = -\frac{8}{3\delta_x}\phi_{x,\frac{1}{2}} + \frac{3}{\delta_x}\phi_{x,1} - \frac{1}{3\delta_x}\phi_{x,2}$, and assuming the variable $q = \delta_x\sqrt{2\beta/k}\cos\theta$, we can recast Eq. (39) as

$$-\tfrac{8}{3}\phi_{x,\frac{1}{2}} + 3\phi_{x,1} - \tfrac{1}{3}\phi_{x,2} = -q\left(\phi_{x,1/2} - \phi^2_{x,1/2}\right), \tag{41}$$

where the subscript x is the horizontal coordinate, $\phi_{x,1/2}$ represents the order parameter at the solid wall which is unknown and needs to be determined. From Eq. (41), we can clearly find that the wall order parameter satisfies the quadratic equation, and it has two solutions, one of which, falling into the region between 0 and 1, will only be used. Once the order parameter at the solid wall is determined, we further use the

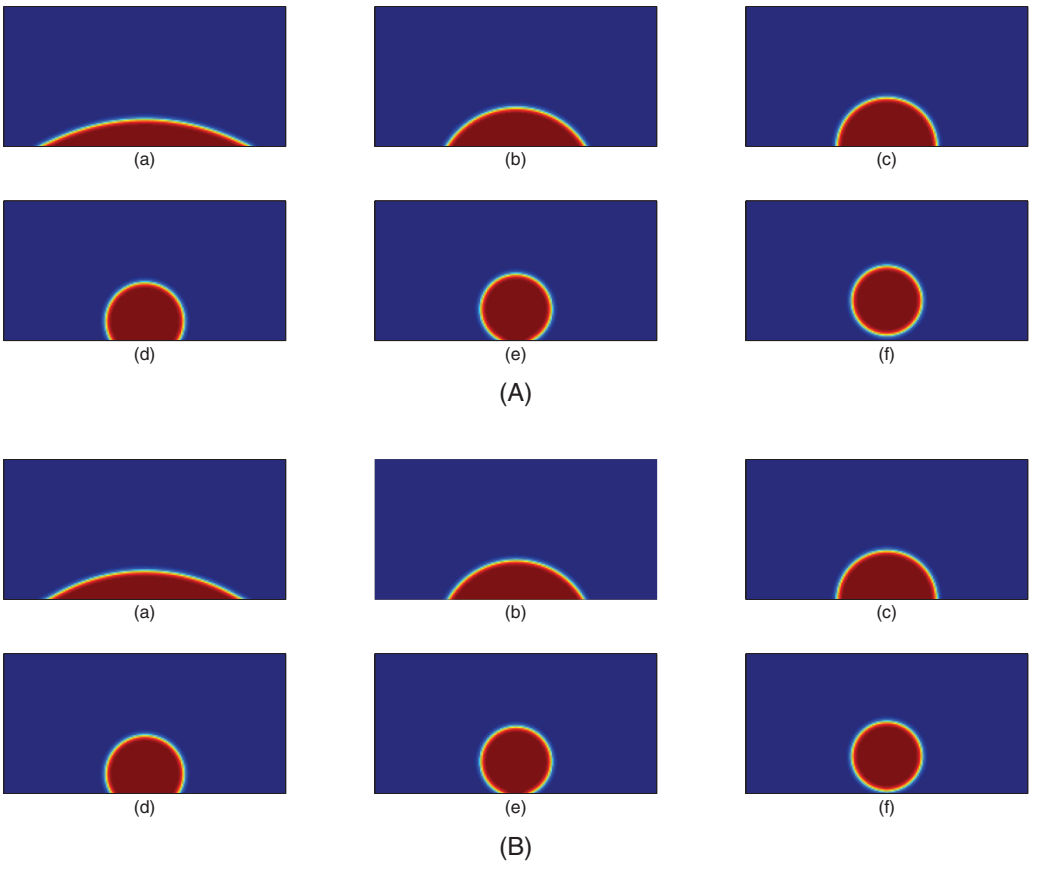

FIG. 2. The predicted droplet equilibrium shapes using the present LB method coupled with the surface-energy (A) and geometrical (B) wetting schemes under conditions of wide range of prescribed contact angles, (a) $\theta = 30^\circ$, (b) $\theta = 60^\circ$, (c) $\theta = 90^\circ$, (d) $\theta = 120^\circ$, (e) $\theta = 150^\circ$, (f) $\theta = 170^\circ$.

second-order interpolation $\phi_{x,0} = 2\phi_{x,1/2} - \phi_{x,1}$ to estimate the value of the order parameter at the ghost node. As a result, the values of $\nabla\phi$ and $\nabla^2\phi$ can be evaluated using Eqs. (25) and (26) in the whole computational domain. Also, we give an illustration on the enforcement of the geometrical wetting boundary condition in the present model. Upon the second-order discretization of Eq. (40), one has

$$\frac{\phi_{x,1} - \phi_{x,0}}{\delta_x} = -\tan\left(\frac{\pi}{2} - \theta\right)|\mathbf{n}_\tau \cdot \nabla\phi|. \tag{42}$$

Equation (42) contains the tangential component of $\nabla\phi$ on the wall, and it can be determined by a second-order extrapolation scheme,

$$\mathbf{n}_\tau \cdot \nabla\phi = \frac{\partial\phi_{x,1/2}}{\partial x} = 1.5\frac{\partial\phi_{x,1}}{\partial x} - 0.5\frac{\partial\phi_{x,2}}{\partial x}, \tag{43}$$

where the derivatives on the right-hand side can be evaluated by a simple second-order central difference approximation,

$$\frac{\partial\phi_{x,y}}{\partial x} = \frac{\phi_{x+1,y} - \phi_{x-1,y}}{2\delta_x}. \tag{44}$$

In this case, the order parameter at the ghost layer can be determined from Eq. (42) and then $\nabla\phi$, $\nabla^2\phi$ in the whole flow region can be calculated. At last, the basic evolution variable in the LB approach is the distribution function, which should also be specified at the physical boundary. For the stationary solid boundary, we apply the halfway bounce back scheme to treat it, which is realized by setting the unknown distribution functions to the ones in the opposite directions. And for the moving boundary, we use the scheme proposed by Ladder [62] to determine the unknown hydrodynamic distribution function,

$$g_{\bar{i}}(\mathbf{x}_f, t) = g_i'(\mathbf{x}_f, t) - 2\omega_i\rho\frac{\mathbf{c}_i \cdot \mathbf{u}_w}{c_s^2}, \tag{45}$$

where $\mathbf{x}_f$ is the fluid node next to solid layer, $\bar{i}$ is the opposite direction of i, g_i' is the postcollision distribution function, and $\mathbf{u}_w$ is the velocity of the moving boundary.

C. Contact angle hysteresis model

The wetting boundary condition presented above is only suitable for describing the wettability of ideal solid wall with a prescribed contact angle. In many realistic fluid-solid systems, the solid surfaces are usually rough and chemically inhomogeneous, and the contact angle hysteresis can play a critical role in influencing contact-line dynamics. Thus it is necessary to construct the contact angle hysteresis model for treating the wettability of nonideal solid surface. Microscopically, the contact angle hysteresis is determined by solid surface inhomogeneities such as the roughness and nonuniformity, and several strategies have been proposed to construct the relations between them at small scale [2,63]. Instead, we implement the contact angle hysteresis directly through the prescription of a receding contact angle θ_R and an advancing contact angle θ_A. If the local contact angle θ lies within a hysteresis window, i.e., $\theta_R < \theta < \theta_A$, the three-phase contact line remains pinned on the wall. Otherwise, if it is beyond the hysteresis window, the contact line is allowed to move along the wall. Specifically, when θ is larger than θ_A, the contact line moves forward and it should move backward when θ is smaller than θ_R. This hysteresis model was proposed by Ding *et al.* [64], who realized it using the geometrical wetting boundary condition, and whether it is applicable for the surface-energy wetting boundary condition remains unknown. For convenience, the simple implementation of the contact angle hysteresis model can be presented as follows. Based on the wetting formulation given in Eqs. (41) or (42), one can derive the initial approximation of the local contact angle θ. Then the comparisons of the local contact angle with the given advancing and receding ones are conducted. If $\theta \leqslant \theta_R$, one should set $\theta = \theta_R$; if $\theta \geqslant \theta_A$, one should set $\theta = \theta_A$; otherwise, θ in the formulation remains unchanged. When θ is obtained according to the above hysteresis rule, one can then update the order parameter in the ghost cell, and the gradient for the order parameter in the entire flow domain can be calculated.

At the end of this section, we would like to give some remarks on the present LB method for contact-line dynamics of binary fluids. The method is built on the conservative Allen-Cahn equation for interface capturing, which contains a lower-order diffusion term compared with the Cahn-Hilliard equation used in the previous phase-field LB models for wetting [36,43,46]. Therefore the present method can achieve a better accuracy and lower numerical dispersion in solving the order parameter, which is a main contribution to handling the high density ratio. Besides the notable difference is that the present method utilizes the second-order isotropic central differences to calculate the derivatives for the order parameter, which can preserve the mass and momentum conservations of a two-phase system, while a mixed scheme combining the central and biased differences is used in the previous phase-field LB models for wetting with the high density ratio [20,36], which has been shown to compromise the conservations of the mass and momentum [42]. Instead of a linear wetting strategy in the LB models [34–37], an advanced cubic surface-energy or geometrical wetting boundary scheme is subtly incorporated in the present method, which would also be useful to improve the method's accuracy and stability for tackling the wetting problem with high density ratio.

III. NUMERICAL RESULTS AND DISCUSSIONS

In this section, we simulate several benchmark examples involving solid surface to validate the wetting boundary treatments in our phase-field LB model. These typical examples include the droplet spreading on an ideal substrate, capillary intrusion, and droplet shearing on the nonideal substrate with the hysteresis. The performances of two popular wetting schemes with a broad range of contact angles are evaluated, and the effects of the linear and inverse schemes used to determine the fluid viscosity across the interface are also discussed. At last, we simulate a three-dimensional microscale droplet impact on a solid substrate, and attempt to compare the present results with the available experiments.

A. Droplet spreading on an ideal wall

A basic two-phase problem of droplet spreading on the ideal wall is first used to verify the developed numerical method [20,27,37,41,43,46,48]. To our knowledge, most of

previous LB simulations [27,41,43,46,48] are restricted to low density ratio and also within a small range of contact angles. In this subsection we will test the model's capability in predicting the wide range of contact angles, and compare them with the prescribed ones. The density ratio (ρ_l/ρ_g) and dynamic viscosity ratio (μ_l/μ_g) considered are 1000 and 100, which approach those of the realistic water-air system at room temperature and normal atmospheric pressure. The simulations are performed in a $N_y \times N_x = 100 \times 200$ rectangular domain, in which a semicircular droplet with the radius $R = 35$ is initially deposited on the bottom wall. To match this setup, the initial distribution profile of the order parameter is given by

$$\phi(x, y) = 0.5 + 0.5 \tanh \frac{2[R - \sqrt{(x - 100)^2 + y^2}]}{W}, \quad (46)$$

which makes its value smooth across the interface. In the simulation, some used physical parameters are set as $\rho_g = 1$, $\nu_g = 0.1, \sigma = 0.2, M = 0.1$. The periodic boundary condition is applied in the horizontal direction, while the no-slip bounce back boundary conditions are imposed at the bottom and top boundaries. To examine the effect of the wall wettability, the wetting boundary scheme should also be used for the bottom boundary. Figure 2 shows the predicted droplet equilibrium shapes using the present LB method coupled with the surface-energy and geometrical wetting schemes under the conditions of the wide range of prescribed contact angles. Here the linear treatment for the kinematic viscosity is applied. From Fig. 2, we can observe that the droplet enables to form different steady patterns on the substrate, which critically depend on the given contact angle. For a hydrophilic wall ($\theta < 90^\circ$), the droplet adheres the substrate surface with a shape of circular cap, while it will shrink on the surface for a hydrophobic wall ($\theta > 90^\circ$). The rough inspection shows that the predicted droplet shapes by two wetting boundary schemes are qualitatively consistent with each other. Further, we also conducted quantitative comparisons between the measured contact angles and the prescribed ones. From the equilibrium pattern of a droplet, we can measure the droplet spreading length between fluid and substrate and its height denoted by L and H. Then based on the geometrical relation $\theta = 2 \arctan 2H/L$, the numerical prediction for the contact angle can be derived. The quantitative comparisons of the surface-energy and geometrical wetting schemes in predicting a board range of contact angles are summarized in Table I, where the linear and inverse forms for viscosity are used, respectively. For very low contact angles of $\theta = 10^\circ$ and $\theta = 15^\circ$, it is noted that the steady droplet has exceeded the grid space, and then we have increased the computational grid to $N_y \times N_x = 100 \times 300$. From Table I, we can find that both the surface-energy and geometrical wetting schemes are able to obtain satisfactory results for the entire range of contact angles from 30° to 150°, of which the maximum absolute errors are almost less than 3°. For the contact angle smaller than 30°, the wall surface is named as superhydrophilic, and it will exhibit the superhydrophobic wetting property for the contact angle larger than 150°. Numerical modeling of the contact angle in such a wetting region is a challenging subject owing to large interface deformation, which probably causes numerical instability. For the contact angle of $\theta = 20^\circ$, it is shown that the results of both wetting schemes are still stable, and the predicted values are overall consistent with the prescribed one. When the contact angle is further decreased, however, we can observe that the geometrical wetting scheme is unstable while the surface-energy wetting scheme can also accurately capture the droplet wetting angle. As for the superhydrophobic case, it is found that the surface-energy scheme can still predict the correct contact angle with better accuracy than that of the geometrical scheme at $\theta = 160^\circ$. But for θ being further increased, both of them work with poor performance, having the large absolute errors of about 10°. The poor prediction at a large contact angle is a well-known problem, and also exists in many numerical approaches [5]. This serious deviation may be attributed to the fact that the droplet achieves a small wetting length on the substrate, which even occupies a considerable size with the interface thickness. As a result, the droplet could be detached from the solid substrate, leading to a large prediction error. As also shown in Table I, we can find that both the linear and inverse methods for the viscosity have comparative accuracy in general for predicting the mild contact angle, regardless of the use of the surface-energy and geometrical wetting formulations. And for the superhydrophilic or superhydrophobic case, it is reported that the linear form for viscosity seems to be more stable than the inverse form.

TABLE I. Comparisons of the surface-energy (A) and geometrical (B) wetting schemes in predicting wide range of contact angles, 'Blanks' mean that the scheme is divergent.

	Scheme A		Scheme B					
Contact angle	linear	inverse	linear	inverse	Absolute errors			
10°	11.3°	11.2°			1.3°	1.2°		
15°	15.4°	15.5°			0.4°	0.5°		
20°	20.7°	19.4°	22.2°		0.7°	0.6°	2.2°	
30°	29.5°	29.4°	30.9°	30.7°	0.5°	0.4°	0.9°	0.7°
45°	43.5°	43.7°	45.4°	45.1°	1.5°	1.3°	0.4°	0.1°
60°	59.1°	59.0°	60.3°	60.2°	0.9°	1.0°	0.3°	0.2°
90°	89.5°	89.2°	89.9°	89.9°	0.5°	0.8°	0.1°	0.1°
120°	120.1°	120.0°	120.6°	120.5°	0.1°	0.0°	0.6°	0.5°
150°	150.9°	151.8°	153.4°	153.1°	0.9°	1.8°	3.4°	3.1°
160°	162.2°	162.7°	166.7°	166.5°	2.2°	2.7°	6.7°	6.5°
165°	180.0°	180.0°	176.2°	180.0°	15.0°	15.0°	11.2°	15.0°
170°	180.0°	180.0°	180.0°		10.0°	10.0°	10.0°	

The existence of parasitic currents at the phase interface is an undesirable numerical artifact inherent in many numerical approaches for two-phase flows. So far, it has been demonstrated that the parasitic currents cannot be completely eliminated in the framework of the LB method. Within this context, to derive small-amplitude spurious velocity is a very rewarding event in the LB community. Here we also investigated the spurious velocity generated by the present LB method coupled with two respective wetting boundary schemes. We can observe that for both cases, the parasitic currents indeed exist at the vicinity of the phase interface, and the streamlines of their velocity fields also show similar patterns near the contact points on the solid surface. In addition, the maximum magnitudes of the spurious velocities

TABLE II. The maximum spurious velocities generated by the present LB method coupled with the surface-energy (A) and geometrical (B) wetting schemes, 'Blanks' mean that the scheme is divergent.

	Scheme A		Scheme B	
Contact angle	linear	inverse	linear	inverse
10°	2.2×10^{-5}	5.0×10^{-5}		
15°	2.6×10^{-5}	5.9×10^{-5}		
20°	2.8×10^{-5}	6.4×10^{-5}	3.7×10^{-5}	
30°	3.6×10^{-5}	6.5×10^{-5}	3.4×10^{-5}	6.1×10^{-5}
45°	2.5×10^{-5}	5.0×10^{-5}	1.7×10^{-5}	2.6×10^{-5}
60°	1.1×10^{-5}	2.1×10^{-5}	1.8×10^{-5}	1.2×10^{-5}
90°	2.2×10^{-6}	7.0×10^{-5}	2.0×10^{-6}	6.0×10^{-6}
120°	1.1×10^{-5}	2.1×10^{-5}	1.0×10^{-5}	1.8×10^{-5}
150°	4.3×10^{-5}	6.7×10^{-5}	1.9×10^{-5}	3.6×10^{-5}
160°	4.8×10^{-5}	7.8×10^{-5}	2.6×10^{-5}	5.3×10^{-5}
165°	5.0×10^{-5}	4.7×10^{-5}	3.0×10^{-5}	2.0×10^{-5}
170°	1.1×10^{-5}	2.0×10^{-5}	3.0×10^{-5}	

are both found to appear at the three-phase junctions, and their values computed by $|\mathbf{u}|_{\max} = (\sqrt{u^2 + v^2})_{\max}$ with two wetting schemes, two viscosity approaches, and various prescribed contact angles are presented in Table II. It can be found that the surface-energy and geometrical wetting schemes used in the present LB method have comparative magnitudes of the spurious velocities, which are also shown to be insensitive to the used viscosity form and the contact angle with the level of 10^{-5}. In this subsection, we further conducted the comparisons between the present method and previously improved LB models for wetting in terms of the spurious velocity. It is reported that the maximum amplitude of spurious velocities in an improved pseudopotential model [27] has the order of 10^{-2}. Recently, Liu *et al.* [48] developed an improved color-gradient based model for high viscosity ratio and density-matched fluids, which produced spurious velocities with the order of 10^{-4}. It is expected that the spurious velocity of the models would increase with the density ratio. In comparison, it is concluded that the present LB method for wetting is able to generate relatively small spurious velocities.

B. Capillary intrusion

Capillary intrusion is a classical contact-line problem for two-phase flows. Due to the existence of the theoretical solution, it can provide a good benchmark for estimating the developed numerical approaches and also has been widely used to assess the proposed multiphase LB models [43,46,48] for simulating moving contact line. To our knowledge, however, all these previous studies only focus on the capillary intrusion processes of low-density-ratio fluids and the models could suffer from the numerical instabilities at high density ratios. In this subsection, we will use the present LB approach to simulate the capillary intrusion flows under a wide range of density ratios, especially tackling the case with the highest density ratio of 1000. Considering a capillary pipe with the size of $L \times H$, where L is the pipe length and H is the width. Initially, the capillary pipe is filled with the gas phase and the outside wetting liquid column would then intrude into the tube. The pioneering work of the capillary intrusion was attributed to Washburn [65], who conducted the theoretical analysis of this problem and gave the well-known law for describing the position of the phase interface,

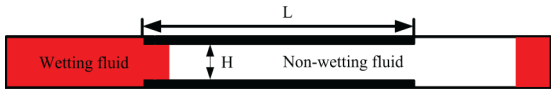

FIG. 3. Schematic of the capillary flow along a pipe.

$$z^2(t) - z^2(0) = \frac{\sigma H \cos(\theta)}{3\mu_l} t, \tag{47}$$

where z is the interface position on the pipe surface, θ is the contact angle, μ_l is the dynamic viscosity of liquid phase, and t is the time. Later, the effects of some other physical factors including the inertial force and the mass of gas phase were incorporated and then the general formulation for predicting the interface position can be expressed by [42,66]

$$[\rho_g(L - z) + \rho_l z]\ddot{z} + (\rho_l - \rho_g)(\dot{z})^2 = 2\frac{\sigma \cos\theta}{H} - \frac{12\dot{z}}{H^2(1 + 6\lambda_s/H)}[\mu_g(L - z) + \mu_l z], \tag{48}$$

where $\ddot{z}$ and $\dot{z}$ denote the first- and second-order derivatives of the interface position z with respect to the time t, μ_g is the dynamic viscosity of the liquid phase, λ_s is a tiny slip length. Generally, the solution of Eq. (48) cannot be given explicitly, but it can be solved numerically using the Runge-Kutta method. If neglecting the gravity and inertial effects, one can simplify the formulation (48) as

$$\sigma \cos\theta = \frac{6}{H}[\mu_g(L - z) + \mu_l z]\dot{z}. \tag{49}$$

As illustrated in Fig. 3, the numerical simulations are performed in the computational domain with the size of $N_x \times N_y = 800 \times 35$, where the capillary pipe occupies the region $200 \leqslant x \leqslant 600$ and the remaining space is periodic in the vertical direction, mimicking an infinite reservoir. Initially, the gas phase is placed in the region $240 \leqslant x \leqslant 750$, and the rest is filled with the liquid fluid. In this case, the length (L) of the pipe occupies 400 lattice units and the initial position of the interface is located at 40. To be smooth across with the interface, the initial distribution for the order parameter in the bulk region is given by

$$\phi(x, y) = 1 - 0.5\left[\tanh\frac{2(x - 240)}{W} - \tanh\frac{2(x - 750)}{W}\right], \tag{50}$$

where the interface width W is set as 5. In our simulations, the used physical parameters for fluids are given as $H = 20$, $\rho_g = 1$, $\nu_l = 0.1$, $M = 0.1$, $\sigma = 0.01$, $\theta = 45°$. The periodic boundary conditions are applied in the horizontal direction, while the no-slip bounce back boundary condition is imposed at the solid wall. In this case, the slip length λ_s should be given as zero. To model the contact angle, the wetting boundary condition is also imposed for the upper and bottom surfaces of the pipe. Four different density ratios of $\rho_l/\rho_g = 1$, 10,

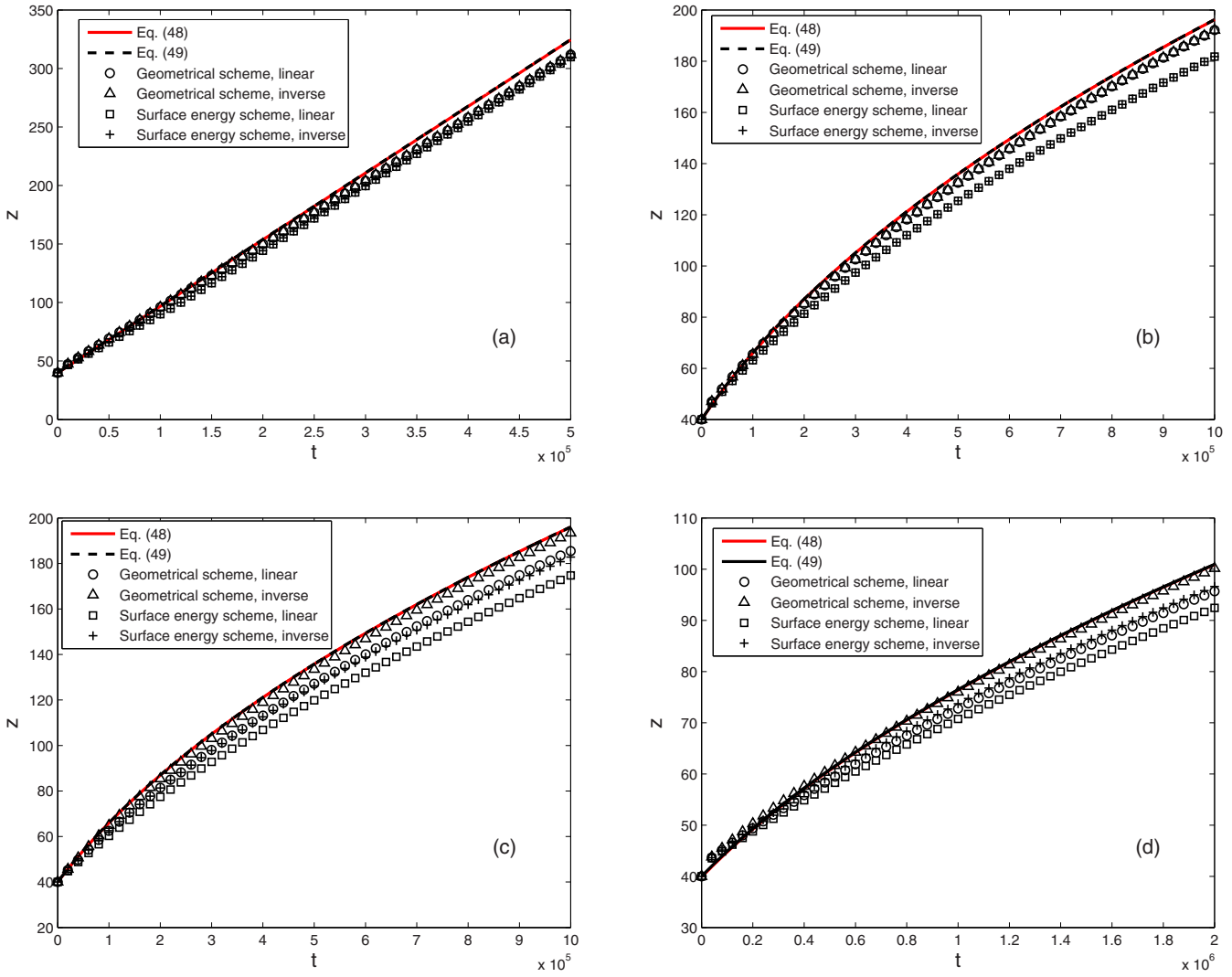

FIG. 4. The predicted interface position in the capillary pipe by the present LB approach with various density ratios: (a) $\rho_l/\rho_g = 1$; (b) $\rho_l/\rho_g = 10$; (c) $\rho_l/\rho_g = 100$; (d) $\rho_l/\rho_g = 1000$.

100, 1000 are considered, where the corresponding kinematic viscosity ratios ν_g/ν_l are 1 for the former two cases, and 10 for the latter two cases. Note that the multiphase system with $\rho_l/\rho_g = 1000$ and $\mu_l/\mu_g = 100$ considered here approaches the realistic water-air system at the normal condition. Figure 4 shows the time evolutions of the interface positions under four typical density ratios, obtained by the present LB approach coupled with two wetting conditions and viscosity schemes. In order to assess the numerical performance, the analytical solutions for predicting the interface position given by Eqs. (48) and (49) are also plotted in Fig. 4. Note that the analytical solutions are presented using the dynamic contact angle for comparisons [41,48,67], and the measured values for four typical density ratios $\rho_l/\rho_g = 1,\ 10,\ 100,\ 1000$ are respectively 46.9, 46.7, 46.8, and 47.6, which are found to be very close but slightly deviate from the prescribed one of 45°. From Fig. 4, we can observe that the profiles of the theoretical solutions line up over each other exactly, which demonstrates the analytical laws (48) and (49) are equivalent for all density ratios. In addition, it can be found from Fig. 4(a) that the present LB approach coupled with the surface-energy and geometrical wetting schemes can correctly capture the position of the intruded liquid interface for a low density ratio of 1. As the density ratio is increased to 10, however, the obvious discrepancy with the analytical solution is found in the result of the surface-energy wetting scheme, and the geometrical wetting scheme can also obtain the satisfactory result. We also consider the cases with high density ratio and viscosity difference, and examined the effect of the used viscosity manner. It can be found from Figs. 4(c) and 4(d) that the surface-energy wetting scheme fails to predict the position of the phase interface, regardless of the use of the linear and inverse treatments for the viscosity. The large deviation can also be observed in the result of the geometrical wetting scheme with linear viscosity form, and conversely, the results of the LB method coupled with the geometrical wetting scheme and inverse manner agree well with the analytical solutions. To further conduct quantitative comparisons, the relative errors of the interface position with different density ratios were measured and the results are summarized in Table III. It can be found that the geometrical wetting scheme can derive a smaller relative error than the surface-energy

TABLE III. The predicted relative errors for the interface location in the capillary pipe using the surface-energy (A) and geometrical (B) wetting schemes and different viscosity schemes.

Wetting models		Viscosity schemes	Density ratios	Absolute errors	
Scheme A	scheme B	linear	1	5.3×10^{-2}	3.1×10^{-2}
Scheme A	scheme B	inverse	1	5.3×10^{-2}	3.1×10^{-2}
Scheme A	scheme B	linear	10	7.2×10^{-2}	2.3×10^{-2}
Scheme A	scheme B	inverse	10	7.2×10^{-2}	2.3×10^{-2}
Scheme A	scheme B	linear	100	11.0×10^{-2}	5.9×10^{-2}
Scheme A	scheme B	inverse	100	6.7×10^{-2}	1.6×10^{-2}
Scheme A	scheme B	linear	1000	6.9×10^{-2}	4.4×10^{-2}
Scheme A	scheme B	inverse	1000	3.4×10^{-2}	8.3×10^{-3}

wetting scheme, and also the inverse method for viscosity is more accurate than the linear one in predicting the dynamic interface position. At the end of this subsection, we can see that the present LB approach coupled with the geometrical wetting scheme and inverse viscosity form can accurately predict the capillary intrusion processes for a wide range of density ratios.

C. Droplet shearing on a nonideal substrate

In this subsection, a droplet on the nonideal substrate subject to a shear flow is investigated to assess the present LB method for simulating contact-line motion with the hysteresis. We intend to conduct a simulation of droplet shearing within the consideration of the contact angle hysteresis at a very high density ratio of 1000, which is unavailable in all previous LB works [46,48]. The physical system considered is a $N_y \times N_x = 128 \times 640$ lattice domain, in which a semicircular droplet with the radius of $R = 64$ is initially attached on the bottom wall centered at the node $(x_c,\ y_c) = (0.3N_x,\ 0)$. The top wall is a moving boundary driven by a horizontal velocity of $U_0 = 0.128$. Periodic boundary conditions are applied in the horizontal direction, while the no-slip and moving bounce back boundary conditions are imposed at the bottom and top boundaries. To account for the hysteresis behavior, the contact angle hysteresis model described above is adopted, and the wetting boundary condition is further used for the bottom boundary. Two popular types of surface-energy and geometrical wetting boundary schemes are respectively chosen, which aims to estimate whether they are suitable for simulating the contact-angle hysteresis phenomenon. The distribution for the order parameter is initialized by

$$\phi(x, y) = 0.5 + 0.5 \tanh \frac{2[R - \sqrt{(x - x_c)^2 + (y - y_c)^2}]}{W}. \tag{51}$$

We first simulate the droplet shearing dynamics with large density and dynamic viscosity ratios of 1000 and 100, which are given by $\rho_l = 1000$, $\rho_g = 1$, $\nu_l = 0.01$, and $\nu_g = 0.1$. The physical properties of binary fluids here are very close to those of the realistic water-air system. The linear form for viscosity is used considering its good stability for simulating various contact angle surfaces. Some remaining physical parameters are fixed to be $\sigma = 2 \times 10^{-4}$ and $M = 0.1$. We choose N_y, U_0 as the characteristic length and velocity, and then the time presented below has been normalized by the characteristic time N_y/U_0. In the current study, four different hysteresis windows $(\theta_R,\ \theta_A)$ are chosen as $(0^\circ,\ 180^\circ)$, $(0^\circ,\ 110^\circ)$, $(70^\circ,\ 180^\circ)$, $(70^\circ,\ 110^\circ)$, which have been recently used by Wang *et al.* [46] and Liu *et al.* [48] for qualitatively testing their LB models, although the density ratios they considered are limited to small ones of 10 and 1, respectively. Figures 5(A) and 5(B) depict the snapshots of droplet shearing processes within four typical hysteresis windows and a high density ratio of 1000, obtained by using the present LB method coupled with the surface-energy and geometrical wetting schemes, respectively. Under the shearing force of the surrounding fluid, the droplet will experience interface deformation or slip along the substrate. Besides, one can expect that four typical motion models of contact points can be derived due to the specified hysteresis regions. For $(\theta_R,\ \theta_A) = (0^\circ,\ 180^\circ)$, both the upstream and downstream dynamic contact angles cannot be beyond the hysteresis window, and thus two contact points in theory always remain pinned on the substrate surface. From Fig. 5(A), we can find that the upstream contact point remains motionless as time goes on, while the downstream contact point displays an undesirable behavior: it moves along the solid surface. This unphysical phenomenon implies that the surface-energy wetting boundary scheme cannot correctly predict the hysteresis of advanced contact angle with the limit value of 180°. In contrast, from Fig. 5(B) we can clearly observe that both upstream and downstream contact points remain immobilized at all times, which indicates that the result obtained by the geometrical wetting boundary scheme is consistent with the theoretical prediction. For $(\theta_R,\ \theta_A) = (0^\circ,\ 110^\circ)$, with the drive of strong shear force, the upstream contact angle changes from its initial right angle to smaller acute ones, which are obviously located in the given hysteresis region $(0^\circ,\ 110^\circ)$. As a result, the upstream contact point should also be fixed, which can be observed in the simulation results of both the surface-energy and geometrical wetting boundary conditions. For the downstream contact point, it is found to be still pinned when the dynamic contact angle is smaller than 110°, and then slips along the solid surface when the increasing dynamic contact angle has been in excess of 110°. The rough inspections show that the surface-energy and geometrical wetting schemes can obtain comparative results in terms of contact-line dynamics for simulating this case. For $(\theta_R,\ \theta_A) = (70^\circ,\ 180^\circ)$, the downstream local contact angle increases continuously from the right angle to the obtuse ones, but it still falls into the set region $(70^\circ,\ 180^\circ)$. Therefore, the downstream contact point in theory cannot move due to the hysteresis, which can be clearly observed in the result of the geometrical wetting boundary scheme. However, it can be found from Fig. 5(A) that the downstream contact point exhibits an unphysical slipping behavior, which demonstrated once again that the surface-energy wetting scheme fails to predict the contact-angle hysteresis phenomenon with the limit value of 180°. For the upstream contact point, it should be pinned at the early stage when the instantaneous contact angle is greater than 70°, and later begins to move downstream when the contact angle is smaller than 70°. However, the above scenario cannot be significantly observed in both results of the surface-energy and geometrical wetting schemes, but instead the upstream

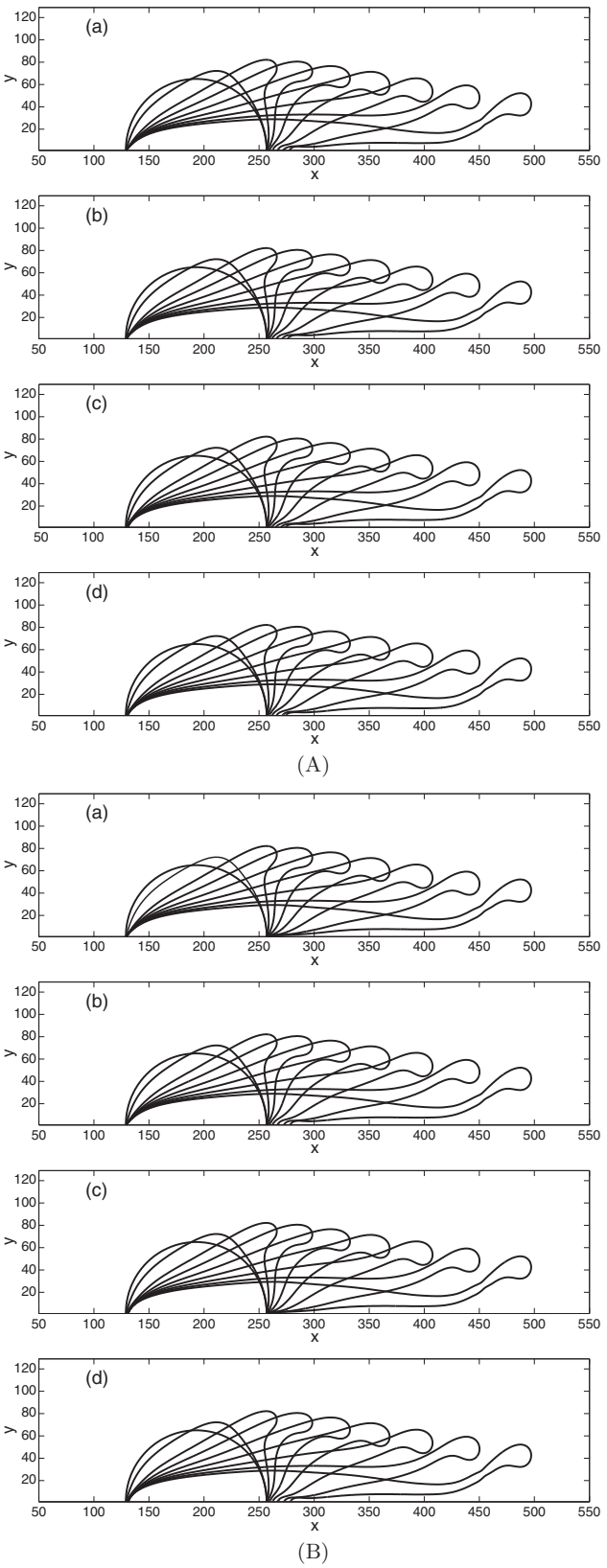

(A)

(B)

FIG. 5. The shearing of a droplet on the substrate using the LB method coupled with the surface-energy (A) and geometrical (B) wetting schemes under different hysteresis windows, $\rho_l/\rho_g = 1000$: (a) $(\theta_R,\ \theta_A) = (0^\circ,\ 180^\circ)$, (b) $(\theta_R,\ \theta_A) = (0^\circ,\ 110^\circ)$, (c) $(\theta_R,\ \theta_A) = (70^\circ,\ 180^\circ)$, (d) $(\theta_R,\ \theta_A) = (70^\circ,\ 110^\circ)$.

contact point always remains immobilized at all times. This anomalous behavior is probably attributed to the fact that the simulated density ratio is extremely large, and thus the contact line of a heavy droplet is very difficult to displace. As expected, if we decrease the density ratio, the upstream contact point will have a remarkable range of motion, which will be demonstrated below. For $(\theta_R,\ \theta_A) = (70^\circ,\ 110^\circ)$, based on the hysteresis rule, we can know that the droplet should keep pinned at the early stage, accompanied by the interface deformation. Subsequently, the local contact angles go beyond the specified hysteresis window and the two contact points begin to slip over the wall. The described behavior for the downstream contact point can be successfully reproduced by both the surface-energy and geometrical wetting schemes, while the obvious motion of the upstream contact point cannot be remarkably observed due to the heavy droplet.

To confirm our above statement, we also conducted some simulations of droplet shearing dynamics with a moderate density ratio of 10. Some detailed physical parameters are given as $\rho_l = 10$, $\rho_g = 1$, $\nu_l = \nu_g = 0.1$, $\sigma = 0.01$, and $M = 0.1$. Figures 6(A) and 6(B) show the patterns of droplet shearing processes on the substrate using the LB method coupled with the surface-energy and geometrical wetting schemes under four hysteresis windows $(0^\circ,\ 180^\circ)$, $(0^\circ,\ 110^\circ)$, $(70^\circ,\ 180^\circ)$, and $(70^\circ,\ 110^\circ)$. For $(\theta_R,\ \theta_A) = (0^\circ,\ 180^\circ)$, it can be found that in the result of the geometrical wetting scheme, the two contact points always remain pinned on the wall, which conforms to the hysteresis rule. Meanwhile, in the result of the surface-energy wetting method, it is shown that the upstream contact point still keeps stationary on the wall, but an unphysical slipping behavior of the downstream contact point is observed due to the method's inadequate capability in simulating the two-phase hysteresis problem with terminal contact angle of 180°. For $(\theta_R,\ \theta_A) = (0^\circ,\ 110^\circ)$, both the surface-energy and geometrical wetting approaches could produce the physically reasonable results, in which the upstream contact point remains fixed and the upstream contact point moves along the solid surface. For $(\theta_R,\ \theta_A) = (70^\circ,\ 180^\circ)$, the upstream contact point is initially pinned since the local contact angle is larger than 70°. Due to the shearing action of the surrounding fluid, the upstream contact angle decreases in time, leading to the motion of the contact point when the contact angle is smaller than 70°. The obvious slipping of the upstream contact point can be observed in this case, which demonstrates our previous statement that the contact line of a light fluid is much easier to be displaced away. As expected, the upstream contact point still remains immobilized in the result of the geometrical wetting approach, while the surface-energy wetting approach fails to predict the correct contact-line behavior under the condition of $\theta_A = 180^\circ$. For the last case of $(\theta_R,\ \theta_A) = (70^\circ,\ 110^\circ)$, both wetting schemes seem to be efficient. It is shown in the figure that the two contact points cannot move at the early stage until the upstream and downstream contact angles reach their hysteresis limits, and then the whole droplet slips over the wall. Different from the case of $\rho_l/\rho_g = 1000$, we can obviously observe that the upstream contact point undergoes an evident slipping, which is consistent with our expectation. From the detailed discussions, we can conclude that both the geometrical and surface-energy wetting approaches

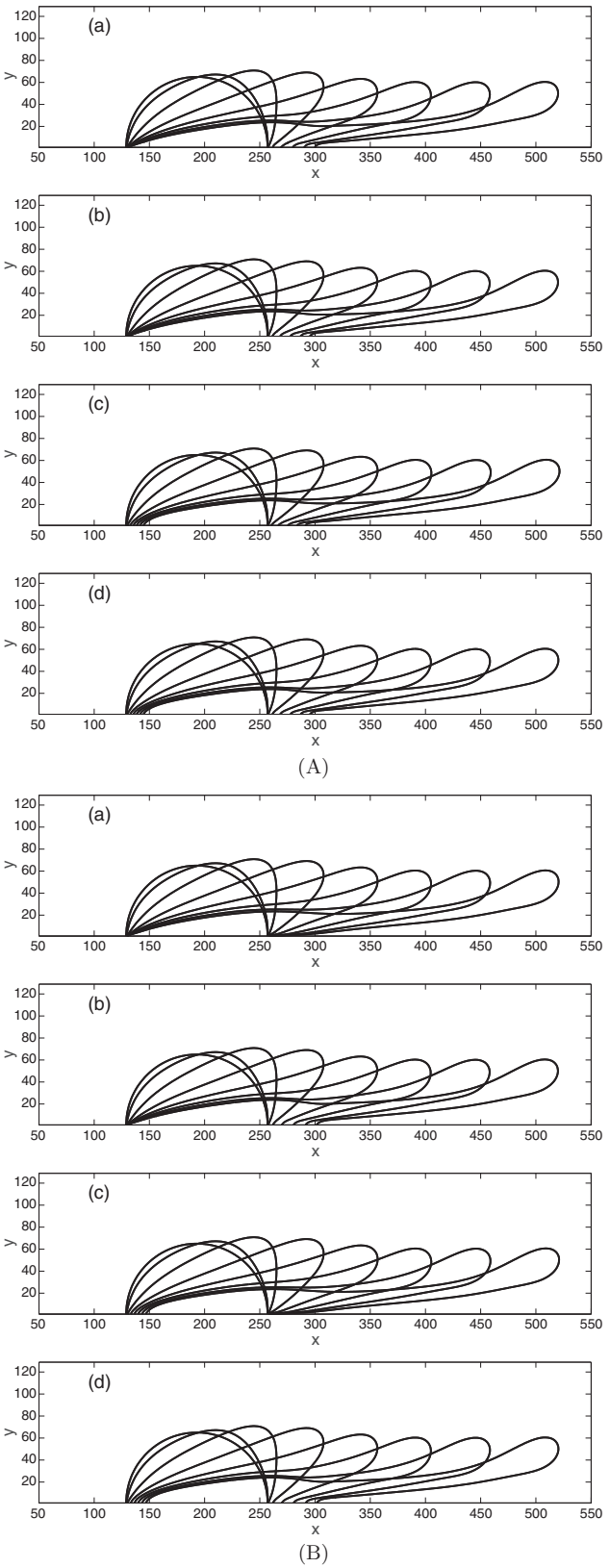

FIG. 6. The shearing of a droplet on the substrate using the LB method coupled with the surface-energy (A) and geometrical (B) wetting schemes under different hysteresis windows, $\rho_l/\rho_g = 10$: (a) $(\theta_R,\ \theta_A) = (0^\circ,\ 180^\circ)$, (b) $(\theta_R,\ \theta_A) = (0^\circ,\ 110^\circ)$, (c) $(\theta_R,\ \theta_A) = (70^\circ,\ 180^\circ)$, (d) $(\theta_R,\ \theta_A) = (70^\circ,\ 110^\circ)$.

can obtain satisfactory results for simulating the contact-line dynamics with the mild hysteresis windows, while the former is more accurate for the extreme advanced contact angle.

D. Droplet impact on a wetting solid

At last, to show the potential of the present model, we consider a extremely complex contact-line problem of micron-scale droplet impact on a wettable solid under the circumstance of high density ratio. Droplet impact on solid surface is a familiar spectacle in the natural event of falling raindrops on the dry ground, and it is also of great importance in numerous engineering applications, such as ink jet printing, plastic electronics, and spray cooling [68]. Owing to complex interfacial dynamics and large density change across the interface, modeling droplet impact poses a great challenge for numerical approaches. In this section, we will use the present LB method to simulate a three-dimensional micron-scale droplet impact on a solid surface with the high density ratio of 844, and compare the numerical results with the experimental data by Dong *et al.* [69]. Before addressing the initial setup of this physical problem, we first recall two main dimensionless parameters characterizing liquid droplet impact processes, namely the Weber number,

$$\mathrm{We} = \frac{\rho_l U_0^2 D_0}{\sigma}, \tag{52}$$

and the Reynolds number,

$$\mathrm{Re} = \frac{U_0 D_0}{\nu_l}, \tag{53}$$

where U_0 is the impact speed of the droplet, and D_0 is its initial diameter used as the characteristic length.

Following the experiment [69], the physical system considered consists of a distilled water droplet on the solid substrate and the surrounding air fluid. The water droplet occupies a microscale size of 48.8 μm, and its impact velocity is 4.36 m/s. The dimensionless Weber and Reynolds numbers are respectively given as $\mathrm{We} = 12.8$ and $\mathrm{Re} = 238$. In the LB simulation, the computational mesh is a $N_z \times N_y \times N_x = 100 \times 200 \times 200$ lattice domain with the periodic boundary conditions in the x and y directions. The bottom plane is the solid wall imposed by the no-slip bounce back boundary condition, while the open boundary condition is applied on the top plane. To be smooth across the interface, the distribution of the order parameter in the whole region is initialized as

$$\phi(x, y, z) = 0.5 + 0.5 \tanh \times \frac{2[R - \sqrt{(x-100)^2 + (y-100)^2 + z^2}]}{W}, \tag{54}$$

where R is the radius of the droplet given by $D_0/2$, and the initial velocity field in the z direction is assigned by

$$(u_x, u_y, u_z) = (0,\ 0,\ -U_0\phi). \tag{55}$$

The densities of the liquid and gas phases in the simulation are set as $\rho_l = 10$ and $\rho_g = 1.1844 \times 10^{-2}$, and their corresponding kinematic viscosities are given by $\nu_l = 0.021$ and

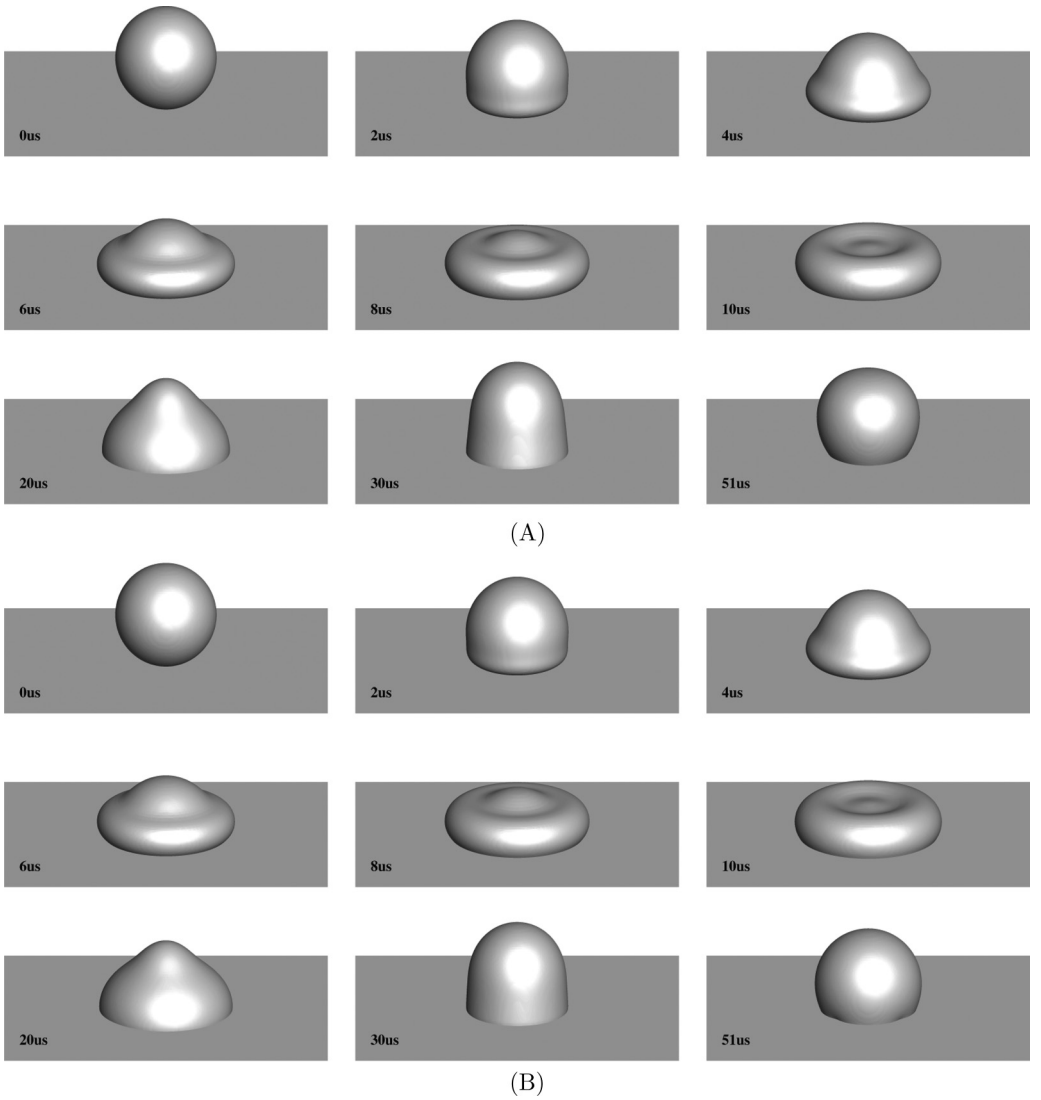

FIG. 7. Snapshots of microscale droplet impact on solid surface obtained by the present LB method coupled with the surface-energy (A) and geometrical (B) wetting schemes, $\theta = 107^\circ$: $\rho_l/\rho_g = 844$ and $\mu_l/\mu_g = 48.5$.

$\nu_g = 0.3659$. Therefore in this study, the density and viscosity ratios of binary fluids are $\rho_l/\rho_g = 844$ and $\mu_l/\mu_g = 48.5$, which closely approach those used in experiments. Some remaining parameters in the simulation are given as $D_0 = 50$, $U_0 = 0.1$, $\sigma = 0.39$, $W = 5$, and $M = 0.1$, and Eq. (23) is used for the viscosity at the interface. Similar to the experimental study [69], two typical wetting properties of the solid surface with the contact angles $\theta = 31^\circ$ and 107° are investigated in this work. Figures 7 and 8 present several typical snapshots of the water droplet impact processes at the contact angles of $\theta = 31^\circ$ and 107°, obtained by the use of the LB approach coupled with the surface-energy and geometrical wetting schemes, respectively. It can be found from Fig. 7 that for the hydrophobic wall, the micron-scale droplet instantly impacts on the substrate surface and its contact area increases with time, which leads to the formation of a droplet shape resembling a truncated sphere at the initial stage. Then, the liquid droplet continues to move radially outward, followed by the visualization of a flat liquid thread at the time 10 μs. After that, the liquid thread begins to contract under the influences of the surface tension force and a classical rebounding phenomenon can be clearly observed in the system. The droplet eventually undergoes a slight oscillation until reaching the equilibrium shape. As for the hydrophilic wall, it can be observed from Fig. 8 that the microscale droplet exhibits similar behaviors as the last case before the time 10 μs. Then the generated liquid thread takes on a distinct appearance, which continues to spread along the substrate and finally forms into a thin liquid film. This droplet behavior can be ascribed to the large adhesive force between the droplet and hydrophilic surface. Further, we can observe from these figures that the surface-energy and geometrical wetting schemes are able to obtain matched numerical results, both of which are qualitatively consistent with the experimental results presented in Fig. 2 of Ref. [69]. Finally, we also give a quantitative study on the droplet spreading radius and height, which are the concerning physical quantities in droplet impact dynamics [20,68,69]. Note that the droplet spreading radius and height here have been normalized by the characteristic length D_0. Figures 9(a) and 9(b) depict the time variations

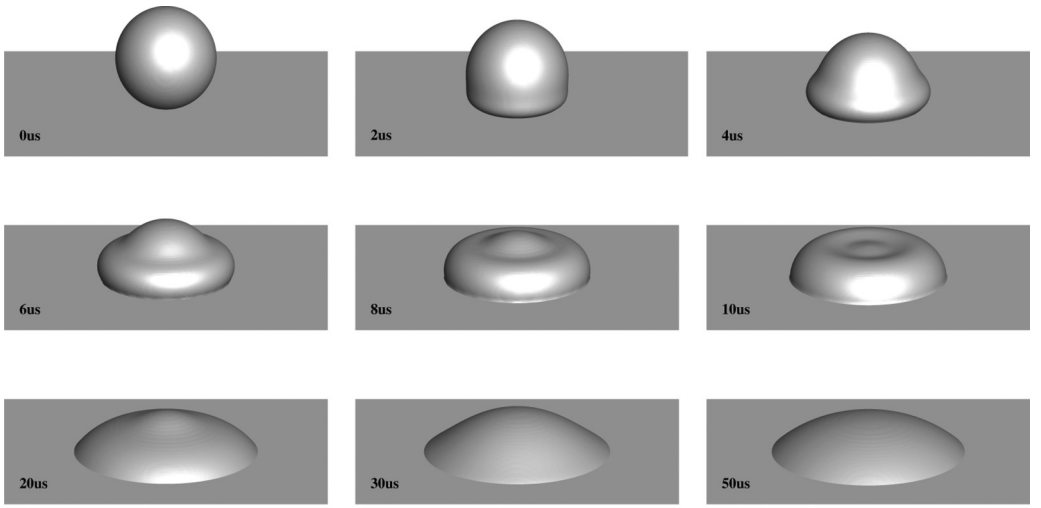

(A)

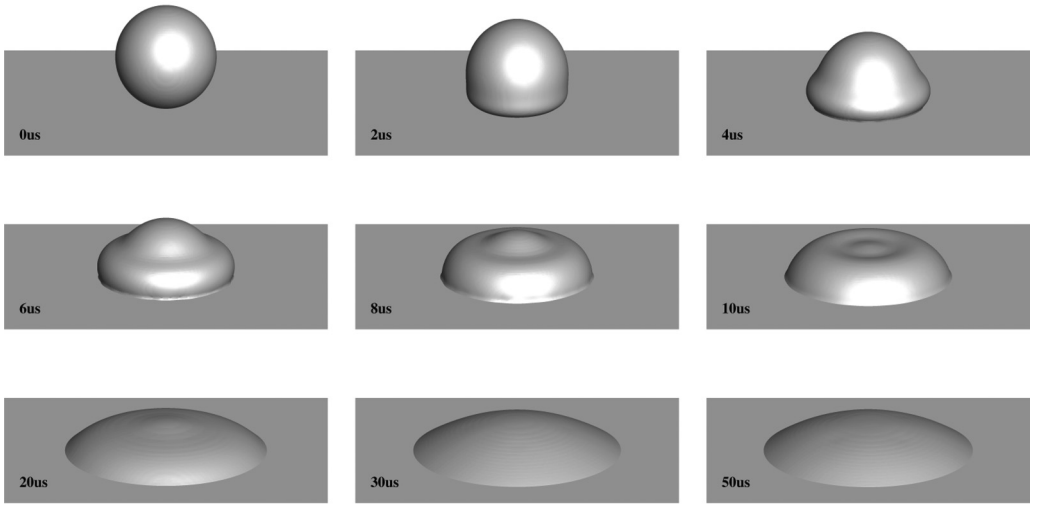

(B)

FIG. 8. Snapshots of microscale droplet impact on solid surface obtained by the present LB method coupled with the surface-energy (A) and geometrical (B) wetting schemes, $\theta = 31^{\circ}$: $\rho_l/\rho_g = 844$ and $\mu_l/\mu_g = 48.5$.

of the spreading ratio D^* and dimensionless droplet height H^* at the contact angles of $\theta = 107^{\circ}$ and 31°, numerically predicted by the present method coupled with the surface-energy and geometrical wetting schemes. For comparisons, the experimental results of Dong *et al.* [69] are also presented. It can be found that the surface-energy and geometrical wetting schemes can obtain the comparative results, both of which show good agreement with the experimental data in general.

IV. SUMMARY

Contact-line dynamic phenomena often arise in nature and scientific researches, but numerical modeling of such flows with high density contrast still remains a challenging task in the LB community. In this paper, we present an improved phase-field LB method for simulating contact-line dynamics on the smooth surface or nonideal surface with contact angle hysteresis, which is able to deal with large density contrasts. To simulate two-phase hydrodynamics, the method takes advantage of double distribution functions for solving the conservative Allen-Cahn and Navier-Stokes equation systems. The conservative Allen-Cahn equation for interface capturing contains a lower-order diffusion term compared with the widely used Cahn-Hilliard equation in the previous LB models. Therefore the present method is expected to gain a better numerical accuracy and stability at high density ratios. Besides, in order to describe solid surface wettability, the derivations of the popular cubic surface-energy and geometric wetting formulations are introduced in detail, and are also carefully incorporated in the framework of the LB approach. Meanwhile, the performance of these wetting boundary conditions are evaluated numerically for a wide range of contact angles. Following the strategy of Ding and Spelt [64], we also conveniently implemented the contact angle hysteresis effect into the present LB method by considering the prescription of a receding contact angle and an advancing contact angle. The method is first validated by simulating two benchmark contact-line problems of droplet spreading on a wettable surface and dynamic capillary intrusion with the highest density

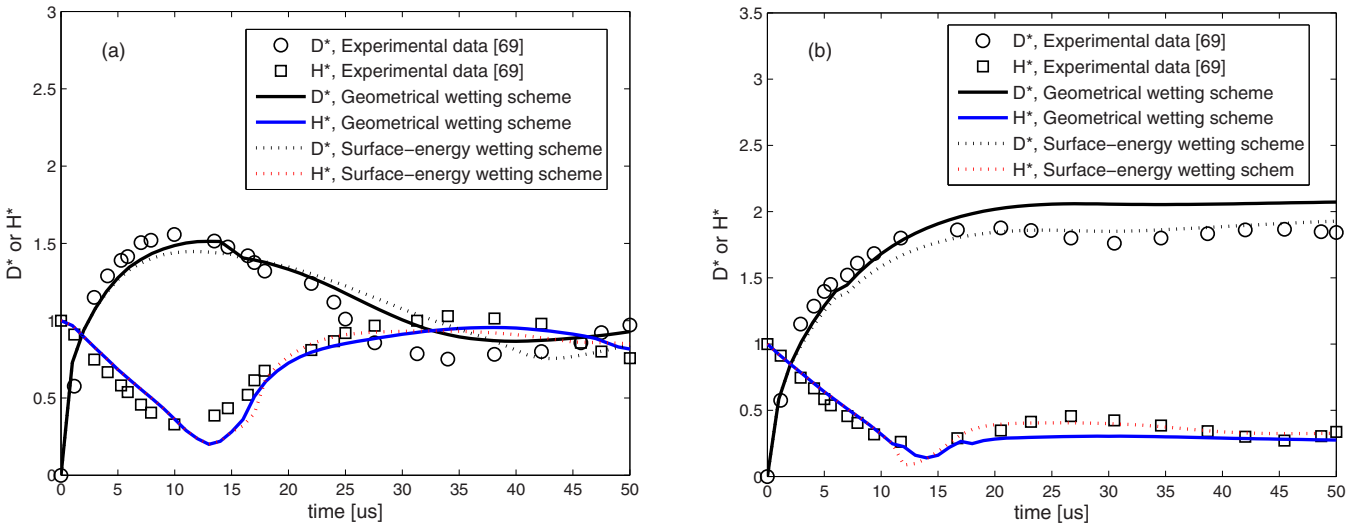

FIG. 9. The time evolutions of the spreading ratio D^* and dimensionless droplet height H^* obtained by the present LB method coupled with surface-energy and geometrical wetting schemes: (a) $\theta = 107^\circ$, (b) $\theta = 31^\circ$.

ratio of 1000. In the former test, it is found that the present methods coupled with the surface-energy and geometrical wetting schemes can obtain satisfactory predictions for the entire range of contact angles between 30° and 150°, while the former scheme is more stable for extremely small contact angles. In addition, it is reported that the present method can derive relatively low spurious velocities compared with other multiphase LB models. In the latter test, we simulated capillary flows with density ratios ranging from 1 to 1000, and also conducted comparisons with the Washburn law. It is found that the present LB approach coupled with the geometrical wetting scheme and inverse viscosity form can accurately predict the capillary intrusion processes for a wide range of density ratios, while some obvious deviations with the Washburn law can be observed in the results of the surface-energy wetting scheme. Subsequently, we also simulated the dynamic behavior of a droplet on the nonideal substrate subject to a shear flow. Four typical motion modes of contact points can be successfully reproduced in the results of the geometrical wetting scheme by adjusting the hysteresis windows. The surface-energy wetting scheme can also derive comparative results within the mild hysteresis windows, while it fails to accurately predict the behavior of downstream contact point for the given advanced contact angle of 180°. Last, to show the method's capability, we simulated a complex contact-line problem of three-dimensional micron-scale droplet impact on a wettable solid under the circumstance of a high density ratio, and compared the numerical results with the experiment. It is found that the present methods coupled with the surface-energy and geometric wetting formulations enable us to derive comparative results in predicting the droplet patterns, spreading radius, and height, all of which show good agreement with the experimental data [69]. In summary, our numerical results indicate that the geometric wetting scheme is slightly more accurate for two-dimensional flows, and the present method is a promising candidate for simulating contact-line dynamics with a broad range of density ratios.

ACKNOWLEDGMENTS

One of the authors (H.L.) gratefully acknowledges insightful discussions with Dr. H. Wang and Dr. X. Yuan. This work was financially supported by the Natural Science Foundation of China (Grants No. 11602075, No. 51776068, No. 61871162), and the Natural Science Foundation of Zhejiang Province (Grant No. LY19A020007).

[1] R. Seemann, M. Brinkmann, T. Pfohly, and S. Herminghaus, Droplet based microfluidics, Rep. Prog. Phys. **75**, 016601 (2012).

[2] P. G. de Gennes, Wetting: Statics and dynamics, Rev. Mod. Phys. **57**, 827 (1985).

[3] R. G. Cox, The dynamics of the spreading of liquids on a solid surface. Part 1. Viscous flow, J. Fluid Mech. **168**, 169 (1986).

[4] J. H. Snoeijer and B. Andreotti, Moving contact lines: Scales, regimes, and dynamical transitions, Annu. Rev. Fluid Mech. **45**, 269 (2013).

[5] Y. Sui, H. Ding, and P. D. M. Spelt, Numerical simulations of flows with moving contact lines, Annu. Rev. Fluid Mech. **46**, 97 (2014).

[6] P. G. de Gennes, A level-set approach for simulations of flows with multiple moving contact lines with hysteresis, J. Comput. Phys. **207**, 389 (2005).

[7] P. Dimitrakopoulos and J. J. L. Higdon, Displacement of fluid droplets from solid surfaces in low-Reynolds-number shear flows, J. Fluid Mech. **336**, 351 (1997).

[8] M. Renardy, Y. Renardy, and J. Li, Numerical smulation of moving contact line problems using a Volume-of-Fluid method, J. Comput. Phys. **171**, 243 (2001).

[9] A. D. Schleizer and R. T. Bonnecaze, Displacement of a two-dimensional immiscible droplet adhering to a wall in shear and pressure-driven flows, J. Fluid Mech. **383**, 29 (1999).

[10] A. Mazouchi, C. M. Gramlich, and G. M. Homsy, Time-dependent free surface Stokes flow with a moving contact line. I. Flow over plane surfaces, Phys. Fluid. **16**, 1647 (2004).
[11] H. Ding and P. D. M. Spelt, Wetting condition in diffuse interface simulations of contact line motion, Phys. Rev. E **75**, 046708 (2007).
[12] Z. L. Guo and C. Shu, *Lattice Boltzmann Method and its Applications in Engineering* (World Scientific, Singapore, 2013).
[13] T. Krüger, H. Kusumaatmaja, A. Kuzmin, O. Shardt, G. Silva, and E. M. Viggen, *The Lattice Boltzmann Method: Principles and Practice* (Springer, Berlin, 2016).
[14] Y. K. Wei, Z. H. Wang, J. F. Yang, H. S. Dou, and Y. H. Qian, A simple lattice Boltzmann model for turbulence Rayleigh-Benard thermal convection, Comput. Fluids **118**, 167 (2015).
[15] Y. K. Wei, Z. D. Wang, and Y. H. Qian, A numerical study on entropy generation in two-dimensional Rayleigh-Benard convection at different prandtl number, Entropy **19**, 443 (2017).
[16] A. K. Gunstensen, D. H. Rothman, S. Zaleski, and G. Zanetti, Lattice Boltzmann model of immiscible fluids, Phys. Rev. A **43**, 4320 (1991).
[17] X. Shan and H. Chen, Lattice Boltzmann model for simulating flows with multiple phases and components, Phys. Rev. E **47**, 1815 (1993).
[18] M. Swift, W. Osborn, and J. Yeomans, Lattice Boltzmann Simulation of Nonideal Fluids, Phys. Rev. Lett. **75**, 830 (1995).
[19] X. He, S. Chen, and R. Zhang, A lattice Boltzmann scheme for incompressible multiphase flow and its application in simulation of Rayleigh-Taylor instability, J. Comput. Phys. **152**, 642 (1999).
[20] T. Lee and L. Liu, Lattice Boltzmann simulations of micron-scale drop impact on dry surfaces, J. Comput. Phys. **229**, 8045 (2010).
[21] H. Liang, B. C. Shi, Z. L. Guo, and Z. H. Chai, Phase-field-based multiple-relaxation-time lattice Boltzmann model for incompressible multiphase flows, Phys. Rev. E **89**, 053320 (2014).
[22] H. Liang, B. C. Shi, and Z. H. Chai, Lattice Boltzmann modeling of three-phase incompressible flows, Phys. Rev. E **93**, 013308 (2016).
[23] V. Sofonea, T. Biciuscă, S. Busuioc, V. E. Ambrus, G. Gonnella, and A. Lamura, Corner-transport-upwind lattice Boltzmann model for bubble cavitation, Phys. Rev. E **97**, 023309 (2018).
[24] N. S. Martys and H. D. Chen, Simulation of multicomponent fluids in complex three-dimensional geometries by the lattice Boltzmann method, Phys. Rev. E **53**, 743 (1996).
[25] R. Benzi, L. Biferale, M. Sbragaglia, S. Succi, and F. Toschi, Mesoscopic modeling of a two-phase flow in the presence of boundaries: The contact angle, Phys. Rev. E **74**, 021509 (2006).
[26] C. E. Colosqui, M. E. Kavousanakis, A. G. Papathanasiou, and I. G. Kevrekidis, Mesoscopic model for microscale hydrodynamics and interfacial phenomena: Slip, films, and contact-angle hysteresis, Phys. Rev. E **87**, 013302 (2013).
[27] Q. Li, K. H. Luo, and X. J. Li, Lattice Boltzmann modeling of multiphase flows at large density ratio with an improved pseudopotential model, Phys. Rev. E **87**, 053301 (2013).
[28] M. Sbragaglia, K. Sugiyama, and L. Biferale, Wetting failure and contact line dynamics in a Couette flow, J. Fluid Mech. **614**, 471 (2008).
[29] S. Varagnolo, D. Ferraro, P. Fantinel, M. Pierno, G. Mistura, G. Amati, L. Biferale, and M. Sbragaglia, Stick-Slip Sliding of Water Drops on Chemically Heterogeneous Surfaces, Phys. Rev. Lett. **111**, 066101 (2013).
[30] H. P. Jansen, K. Sotthewes, C. Ganser, H. J. W. Zandvliet, C. Teichert, and E. S. Kooij, Shape of picoliter droplets on chemically striped patterned substrates, Langmuir **30**, 11574 (2014).
[31] J. F. Zhang and D. Y. Kwok, Lattice Boltzmann study on the contact angle and contact Line dynamics of liquid-vapor interfaces, Langmuir **20**, 8137 (2004)
[32] A. Mazloomi, M. S. S. Chikatamarla, and I. V. Karlin, Entropic lattice Boltzmann method for multiphase flows: Fluid-solid interfaces, Phys. Rev. E **92**, 023308 (2015).
[33] J. W. Cahn, Critical point wetting, J. Chem. Phys. **66**, 3667 (1977).
[34] A. J. Briant, Lattice Boltzmann simulations of contact line motion in a liquid-gas system, Philos. Trans. R. Soc. London A **360**, 485 (2002).
[35] A. J. Briant, A. J. Wagner, and J. M. Yeomans, Lattice Boltzmann simulations of contact line motion. I. Liquid-gas systems, Phys. Rev. E **69**, 031602 (2004).
[36] T. Lee and L. Liu, Wall boundary conditions in the lattice Boltzmann equation method for nonideal gases, Phys. Rev. E **78**, 017702 (2008).
[37] Y. Y. Yan and Y. Q. Zu, A lattice Boltzmann method for incompressible two-phase flows on partial wetting surface with large density ratio, J. Comput. Phys. **227**, 763 (2007).
[38] N. Moradi, F. Varnik, and I. Steinbach, Roughness-gradient-induced spontaneous motion of droplets on hydrophobic surfaces: A lattice Boltzmann study, Europhys. Lett. **89**, 26006 (2010).
[39] R. J. Vrancken, M. L. Blow, H. Kusumaatmaja, K. Hermans, A. M. Prenen, C. W. M. Bastiaansen, D. J. Broer, and J. M. Yeomans, Anisotropic wetting and de-wetting of drops on substrates patterned with polygonal posts, Soft Matter **9**, 674 (2013).
[40] H. Kusumaatmaja, E. J. Hemingway, and S. M. Fielding, Moving contact line dynamics: From diffuse to sharp interfaces, J. Fluid Mech. **788**, 209 (2016).
[41] H. S. Wiklund, S. B. Lindstrom, and T. Uesaka, Boundary condition considerations in lattice Boltzmann formulations of wetting binary fluids, Comput. Phys. Commun. **182**, 2192 (2011).
[42] Q. Lou, Z. L. Guo, and B. C. Shi, Effects of force discretization on mass conservation in lattice Boltzmann equation for two-phase flows, Europhys. Lett. **99**, 64005 (2012).
[43] Q. Lou, M. Yang, and H. Xu, Wetting boundary condition in an improved lattice Boltzmann method for nonideal gases, Commun. Comput. Phys. **23**, 1116 (2018).
[44] M. Latva-Kokko and D. H. Rothman, Static contact angle in lattice Boltzmann models of immiscible fluids, Phys. Rev. E **72**, 046701 (2005).
[45] M. Latva-Kokko and D. H. Rothman, Scaling of Dynamic Contact Angles in a Lattice-Boltzmann Model, Phys. Rev. Lett. **98**, 254503 (2007).
[46] L. Wang, H. B. Huang, and X. Y. Lu, Scheme for contact angle and its hysteresis in a multiphase lattice Boltzmann method, Phys. Rev. E **87**, 013301 (2013).
[47] Y. Ba, H. Liu, J. Sun, and R. Y. Zheng, Color-gradient lattice Boltzmann model for simulating droplet motion with contact-angle hysteresis, Phys. Rev. E **88**, 043306 (2013).

[48] H. Liu, Y. Ju, N. Wang, G. Xi, and Y. Zhang, Lattice Boltzmann modeling of contact angle and its hysteresis in two-phase flow with large viscosity difference, Phys. Rev. E **92**, 033306 (2015).

[49] D. Jacqmin, Calculation of two-phase Navier-Stokes flows using phase-field modeling, J. Comput. Phys. **155**, 96 (1999).

[50] P. H. Chiu and Y. T. Lin, A conservative phase field method for solving incompressible two-phase flows, J. Comput. Phys. **230**, 185 (2011).

[51] F. Ren, B. W. Song, M. C. Sukop, and H. B. Hu, Improved lattice Boltzmann modeling of binary flow based on the conservative Allen-Cahn equation, Phys. Rev. E **94**, 023311 (2016).

[52] H. Liang, J. R. Xu, J. X. Chen, H. L. Wang, Z. H. Chai, and B. C. Shi, Phase-field-based lattice Boltzmann modeling of large-density-ratio two-phase flows, Phys. Rev. E **97**, 033309 (2018).

[53] H. Liang, Y. Li, J. X. Chen, and J. R. Xu, Axisymmetric lattice Boltzmann model for multiphase flows with large density ratio, Int. J. Heat Mass Transfer **130**, 1189 (2019).

[54] Y. K. Wei, Z. D. Wang, H. S. Dou, Y. H. Qian, and W. W. Yan, Simulation of natural convection heat transfer in an enclosure at different Rayleigh number using lattice Boltzmann method, Comput. Fluids **124**, 30 (2016).

[55] H. Liang, B. C. Shi, and Z. H. Chai, An efficient phase-field-based multiple-relaxation-time lattice Boltzmann model for three-dimensional multiphase flows, Comput. Math. Appl. **73**, 1524 (2017).

[56] Y. K. Wei, Z. D. Wang, H. S. Dou, and Y. H. Qian, A novel two-dimensional coupled lattice Boltzmann model for incompressible flow in application of turbulence Rayleigh-Taylor instability, Comput. Fluids **156**, 97 (2017).

[57] Y. K. Wei, H. Yang, H.-S. Dou, Z. Lin, Z. Wang, and Y. Qian, A novel two-dimensional coupled lattice Boltzmann model for thermal incompressible flows, Appl. Math. Comput. **339**, 556 (2018).

[58] Z. L. Guo, C. G. Zheng, and B. C. Shi, Discrete lattice effects on the forcing term in the lattice Boltzmann method, Phys. Rev. E **65**, 046308 (2002).

[59] J. Kim, A continuous surface tension force formulation for diffuse-interface models, J. Comput. Phys. **204**, 784 (2005).

[60] M. R. Moldover and J. W. Cahn, An interface phase transition: Complete to partial wetting, Science **207**, 1073 (1980).

[61] T. Young, An essay on the cohesion of fluids, Philos. Trans. R. Soc. London **95**, 65 (1805).

[62] A. J. C. Ladd, Numerical simulations of particulate suspensions via a discretized Boltzmann equation. Part 1. Theoretical foundation, J. Fluid Mech. **271**, 285 (1994).

[63] R. Tadmor, Line energy and the relation between advancing, receding, and Young contact angles, Langmuir **20**, 7659 (2004).

[64] H. Ding and P. D. M. Spelt, Onset of motion of a three-dimensional droplet on a wall in shear flow at moderate Reynolds numbers, J. Fluid Mech. **599**, 341 (2008).

[65] E. W. Washburn, The dynamics of capillary flow, Phys. Rev. **17**, 273 (1921).

[66] F. Diotallevi, L. Biferale, S. Chibbaro, A. Lamura, G. Pontrelli, M. Sbragaglia, S. Succi, and F. Toschi, Capillary filling using lattice Boltzmann equations: The case of multi-phase flows, Eur. Phys. J.: Spec. Top. **166**, 111 (2009).

[67] C. M. Pooley, H. Kusumaatmaja, and J. M. Yeomans, Modelling capillary filling dynamics using lattice Boltzmann simulations, Eur. Phys. J.: Spec. Top. **171**, 63 (2009).

[68] A. L. Yarin, Drop impact dynamics: Splashing, spreading, receding, bouncing..., Annu. Rev. Fluid Mech. **38**, 159 (2006).

[69] H. Dong, W. W. Carr, D. G. Bucknall, and J. F. Morris, Temporally-resolved inkjet drop impaction on surfaces, AIChE J. **53**, 2606 (2007).